JOURNAL OF AIRCRAFT
Vol. 47, No. 2, March–April 2010

Interaction of Synthetic Jet with Boundary Layer Using Microscopic Particle Image Velocimetry

Manikandan Ramasamy*
NASA Ames Research Center, Moffett Field, California 94035
and
Jacob S. Wilson† and Preston B. Martin‡
NASA Langley Research Center, Hampton, VA 23681

DOI: 10.2514/1.45794

The aerodynamic interaction between an unsteady, inclined synthetic jet and a crossflow boundary layer was studied as a precursor toward applying active flow control concepts for rotor applications, such as dynamic stall control and fuselage drag reduction. Because the flowfield offered numerous challenges from a measurement perspective, several experiments were carried out using a phase-locked, two-dimensional microscopic particle image velocity technique in a building block approach, by adding one complexity after another. The procedure began with boundary layer measurements made on a simple flat plate using the microscopic particle image velocity technique. Velocity measurements were made deep in the viscous sublayer, as close as 20μm from the surface. Following this, the synthetic jet actuator was characterized while operating in quiescent air as well as in crossflow. The results showed that the evolution of the synthetic jet in crossflow was substantially different from its evolution in quiescent air, suggesting that any flow physics or performance prediction (for example, the depth of penetration of the jet into the boundary layer) made based on the quiescent flow conditions may not be applicable in crossflow. All the momentum added to the boundary layer had its source from the synthetic jet actuator, and the penetration of the jet was limited to the viscous sublayer and log layer; the outer layer was unaffected, despite using a jet to freestream velocity ratio of four. Significant effort was also made to validate the microscopic particle image velocity technique and evaluate its capability to accurately resolve such a complex flowfield. To this end, microscopic particle image velocity measurements were compared with hot-wire measurements made on a simple steady jet, as well as an unsteady, periodic synthetic jet. Excellent correlation was found between the two techniques, validating microscopic particle image velocity measurements.

Nomenclature

A = rotor disk area, m^2
b = width of the actuator slot
D = diameter of the steady jet nozzle, m
f_e = effective flat plate area, m^2
H = momentum flux deficit, Nm^{-1}
l = distance from the leading edge of the flat plate
N = number of vectors skipped to avoid image congestion
R = range of a helicopter
r = radial distance, m
U = axial velocity of the jet, ms^{-1}
$\langle U \rangle$ = absolute velocity, $\sqrt{U^2 + V^2}$
U_{Jet} = designated axial velocity of the jet
$U_{\max}$ = peak axial velocity, ms^{-1}
U^+ = nondimensional streamwise velocity, u/u^*
u = streamwise velocity, ms^{-1}
u_0 = freestream velocity, ms^{-1}
u^* = friction velocity
V = radial velocity of the jet, ms^{-1}
VR = velocity ratio, $U_{\mathrm{Syn.Jet}}/U_\infty$
X = axial coordinate of the jet
x = streamwise coordinate of the wind tunnel
Y = radial coordinate of the jet
Y^+ = nondimensional wall normal distance, yu^*/ν
y = wall normal coordinate of the wind tunnel
Z = out-of-plane coordinate of the jet
z = out-of-plane coordinate of the wind tunnel
δ = thickness of the boundary layer, m
δ_b = thickness of a laminar boundary layer, m
δ_{turb} = thickness of a turbulent boundary layer, m
δ^* = displacement thickness of the boundary layer, m
ζ = phase of the actuator signal, deg.
θ = momentum thickness of the boundary layer
κ = von Kármán constant
μ-PIV = microscopic particle image velocity
ν = kinematic viscosity
ρ = air density, kg m^{-3}

Introduction

CONSIDERABLE effort has been spent in the past several decades to improve helicopter performance and, in turn, extend the operational flight envelope [1–4]. The goals include increased maximum speed, range, and endurance, as well as enhancing maneuvering envelopes in forward flight while reducing rotor vibration and noise.

Using a generic military helicopter as an example, Martin et al. [5] derived an expression relating the sensitivity of the maximum range of a helicopter to the changes in its flat plate area (changes in drag) as

---

Received 3 June 2009; revision received 17 August 2009; accepted for publication 18 August 2009.

*Research Scientist, University of California at Santa Cruz; mani.ramasamy@us.army.mil. Member AIAA.

†Research Scientist, Aeroflightdynamics Directorate, U.S. Army Research, Development, and Engineering Command; jacob.s.wilson@us.army.mil.

‡Research Scientist, Aeroflightdynamics Directorate, Joint Research Program Office, U.S. Army Research, Development, and Engineering Command; preston.b.martin@us.army.mil.

$$\frac{\Delta R_{\max}}{R_{\max}} \approx \frac{1}{2}\frac{\Delta(f_e/A)}{(f_e/A)} \tag{1}$$

where f_e is the effective flat plate area, and A is the rotor disk area. At the best-range speed (after taking into account the increase in the best-range speed associated with a reduction in drag), a 30% reduction in drag was shown to provide only a 12% increase in the maximum range. This illustrates the need for a substantial reduction in drag if the goal is to achieve a significant improvement in the range. Similarly, continuous improvements in engines (and transmission) have enabled previously power-limited helicopters that operate in high-altitude to reach the stall boundary before reaching the limitations of power [6]. Although reducing drag and extending the stall boundary have been subjects of active research for the past several decades, recent advances in active flow control (AFC) concepts suggest that they have a potential to play a valuable role in overcoming these aerodynamic hurdles.

AFC devices have been widely used to energize boundary layers when adverse pressure gradients cause flow separation. This is achieved by increasing fluid momentum in the boundary layer through enhanced turbulent mixing, steady mass injection, or suction of low-momentum fluid through the surface. Early efforts in applying AFC to rotor applications used steady blowing, and were found to result in some performance benefits. The power required and complexity of the systems, however, keeps the concept from being feasible for a flight vehicle. Modern studies have shown that unsteady flow control by synthetic jets can be more effective than steady methods for a given momentum input [7,8]. For example, unsteady AFC systems have been successfully applied toward controlling dynamic stall [9] and in fuselage drag reduction [10].

In spite of this progress, state-of-the-art synthetic jet (unsteady) flow control techniques still suffer from the earliest problems of predicting the required momentum input, optimum frequency of unsteadiness, and placement of the flow control orifice to maximize the system performance on an untested problem. Synthetic jets interact with a boundary layer through two mechanisms. First, by directly pulling low-speed fluid into the actuator and pumping out high-speed fluid into the shear layer; the actuator acts as a momentum source. Second, appropriate tuning of the actuator frequency can excite instabilities in the shear layer that, in turn, cause large-scale coherent structures to bring high-momentum fluid from the mean flow into the boundary layer. The effectiveness of this mechanism, however, is highly dependent on the location of the actuator slot with respect to the location at which the flow separates.

These two mechanisms do not necessarily operate independently and have often been shown to be interrelated [11]. Provided with an appropriate placement of the actuator slot (near the point of separation) and excited with correct frequency, only a small fraction of momentum may be needed to reattach the flow. These interdependencies need to be understood from a flow physics standpoint if the final goal is to systematically develop and optimize future AFC systems for rotorcraft. This will directly depend on developing accurate fundamental knowledge of the aerodynamic interaction between the unsteady actuator jet and the boundary layer, especially near the slot exit. This is a daunting problem in itself even in the case of a simple 2-D airfoil model. For dynamic rotorcraft testing there are even more significant challenges that are now being explored for the first time. Current and future AFC dynamic stall and rotor tests need a measurement technique that can unobtrusively resolve the boundary-layer flowfield and explain the flow physics of dynamic stall delay through AFC techniques.

Substantial work has been done in the past decade toward characterizing AFC actuators and optimizing flow control systems through both computational fluid dynamic (CFD) simulations [12] and experimental measurements [13–16]. A wide variety of synthetic jets of varying sizes (0.9-mm–125-mm) and shapes (circular, elliptical, and rectangular), operating at a wide range of Reynolds numbers and Mach numbers have been analyzed using different measurement techniques. These include hot-wire anemometry (HWA), laser Doppler velocimetry (LDV), and particle image velocimetry (PIV). Different kinds of actuating mechanisms that include peizoelectric, peizoceramic, solenoid, and simple acoustic speakers have been tried at operating frequencies in the range of 1–4000-Hz. In the case of rectangular and elliptic jet configurations, the orientation of the slots with respect to the freestream flow (yaw) have been studied in detail. However, one common feature among most of the synthetic jet experiments performed in the past, which is different in the present study, has been the inclination of the jet axis with respect to the exit plane. Whereas most of the studies were made on jets blowing normal to the exit plane, the present work uses synthetic jets that blow at approximately 50 deg to the exit plane. The advantages of using an inclined synthetic jet can be found in [17,18]. However, very limited studies exist on characterizing an inclined synthetic jet [17–20].

One of the biggest shortcomings for both CFD and experiments (irrespective of the choice of the synthetic jet actuator used) has been the inadequate spatial resolution. This is understandable considering the thickness of the boundary layer (~2–3-mm) at large Reynolds numbers that are found in full-scale helicopter rotors. Similarly, the physical dimensions of the actuator jets that are often used to control the flow are typically of the order of very few millimeters and have very high velocities (of the order of freestream flow). This means that the velocity gradients are very high.

Consequently, grid sizes of the order of tens or, at least, low hundreds of microns are necessary to resolve the flow accurately. This involves significant computing time. Furthermore, the actuator jet also produces small-scale coherent structures that are even smaller than the jet itself. The interaction between these structures and the boundary layer is the key to understanding the flow physics of active flow control. Despite these challenges, CFD simulations are routinely used to provide the first iteration on AFC design by, for example, predicting the spatial location at which the actuator may be placed. Although this is valuable information, the poor confidence level in CFD predictions when the flow experiences significant adverse pressure gradient prevents it from being a reliable predictive tool.

Measurement Challenges

Understanding the aerodynamic interaction between the synthetic jet and the boundary layer involves solving several experimental challenges (Fig. 1) that require specific instrumentation capabilities. The challenges include 1) measuring the high-velocity gradients exhibited by the synthetic jets, especially at their edges, 2) resolving small-scale, rotational coherent structures (such as lip vortices) produced in the flow because of the shear between the jet and the freestream, 3) characterizing the boundary layer accurately, and 4) performing phase-resolved measurements that are synchronized with the actuator excitation signal.

While the first two challenges require the capability to perform measurements at high-spatial resolution [21–23], the second challenge also requires the measurement technique to be free of directional ambiguity. The third challenge demands measurements to be made as close to the surface as possible, especially near the wall, where the velocity gradients have been proven to be nonlinear. Finally, the fourth challenge helps to characterize the time evolution of the coherent structures released by the unsteady, periodic synthetic jet, as well as their interaction with the boundary layer. A measurement technique with the previously mentioned capabilities is key to fully understanding the physical process of AFC.

A critical parameter underlying the first three requirements is the size of the measurement volume. This is defined by the physical dimensions of the probe itself and plays the primary role in determining the accuracy of the measured velocities. The size of the measurement volume should be as small as possible and is the key to accurately resolving high-velocity gradient flow fields. This is understandable considering that the velocity gradient within the measurement volume gets averaged.

Among the available measurement techniques, HWA has the smallest measurement volume. Defined by the diameter of the probe, it is of the order of ~3-μm. Although this satisfies the first requirement comfortably, using HWA for characterizing boundary layers with AFC has significant disadvantages. This is because of the inherent ambiguity in resolving the flow direction, thus failing to

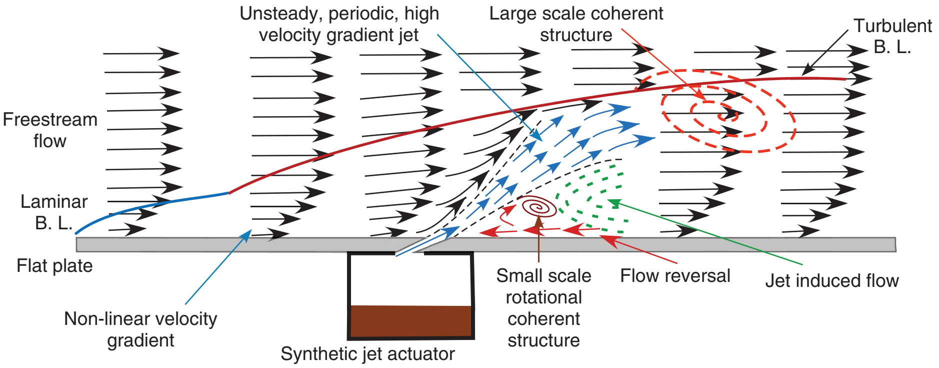

Fig. 1 **Challenges in understanding the interaction between a synthetic jet and a boundary layer.**

satisfy the second condition. Also, accurately, repeatably, and safely placing a physical probe near an oscillating or rotating wing model is impractical. This directly points to nonintrusive, optical measurement techniques such as LDV or PIV.

The measurement volume for LDV is defined by a small region that is common to all six coincident beams. With good alignment, this size is of the order of ~80-μm [24,25]. Even though the measurement volume of LDV is one order larger than hot wires, it might still be considered acceptable for the flow under consideration. Also, LDV satisfies all the requirements. However, because LDV is a point measurement technique, these benefits are countered by the large time consumed to perform a set of measurements in a given plane. Also, reconstructing the velocity field to understand the evolution of coherent structures inside the boundary layer will be challenging.

PIV, on the other hand, measures the velocity field over a plane at a given instant of time, allowing studies on the time varying interaction between the synthetic jet and the boundary layer to be conducted with considerable ease [26–29]. Here, the size of the interrogation window in the physical dimension defines the size of the measurement volume. Historically, the main problem with PIV technique has been the size of its measurement volume, despite continuous improvements in camera resolution. Even though it satisfies all the aforementioned requirements, the size of the measurement volume has been its Achilles heel. In the present study, this shortcoming has been overcome by significantly reducing the region of interest (viewing area) through the application of a microscope instead of a conventional optical lens. Consequently, the size of the measurement volume is reduced considerably (~40-μm), making it suitable for the current application. The term μ-PIV has been used because the size of the viewing area is smaller than the imaging CCD, meaning that the magnification is greater than one.

With the PIV technique, reducing the size of the measurement volume has an added advantage in terms of the accuracy of measured velocity. Other than velocity gradient being averaged within the measurement volume (discussed earlier), PIV measurements suffer from velocity gradient bias error when applied to a flowfield containing high-velocity gradients. This is because of the better correlation occurring at lower-velocity regions within the interrogation window that biases the measured velocity to lower values. Smaller interrogation windows have proven to resolve the velocity gradients better than the larger windows. Furthermore, it should be understood that the size of the measurement volume defines how close measurements can be made to the surface, which is essential to understanding the interaction between the synthetic jet and the flow inside the boundary layer.

A key issue, however, is that the capability of μ-PIV to resolve high-velocity gradient jets that are filled with small-scale rotational coherent structures remains to be fully evaluated. This is an essential intermediate step before applying it to understand the interaction between the synthetic jet and a boundary layer; otherwise the new observed physics may not derive from the flow, but from the instrumentation technique itself.

The objective of the present work is twofold. First, to assess and validate the capability of μ-PIV technique to accurately resolve a nonlinear, high-velocity gradient flowfield that is filled with small-scale rotational coherent structures. Toward this end, two validation tests were conducted. Second, to perform μ-PIV measurements that will help to understand the aerodynamic interaction between the synthetic jet and the boundary layer. This was achieved by conducting experiments on a flat plate with zero pressure gradient and by characterizing an unsteady, periodic synthetic jet operating in still air, as well as in crossflow. By comparing the streamwise velocity distribution, momentum flux deficit, and the evolution of coherent structures inside the boundary layer among the three measurements, it was possible to develop an understanding of the aerodynamic interaction between the synthetic jet actuator (SJA) and the boundary layer. This, in turn, helped to identify key parameters that will play a significant role in improving the effectiveness of SJA for flow control applications.

Methodology

Figure 2 shows the sequence of measurements that were performed in the present study. These include two validation tests to evaluate the capabilities of μ-PIV and three measurements to understand the aerodynamic interaction between the synthetic jet and a boundary layer.

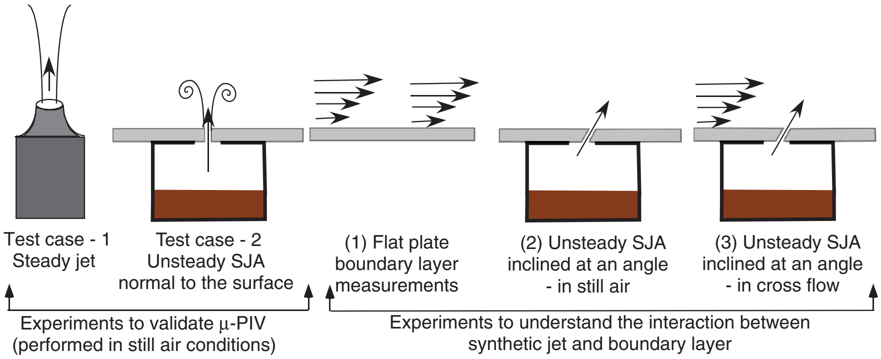

Fig. 2 **Sequence of measurements made in the present study.**

Test Case 1

Here, μ-PIV measurements were made in a steady blowing axisymmetric jet in quiescent air at two different velocities (15-m/s and 50-m/s). This experiment validated the capability of μ-PIV technique to accurately resolve the high-velocity gradients. The jet was provided by a calibration system that is usually used to calibrate hot wires. More details of the system are given in the section explaining the experimental setup. A steady axisymmetric jet was chosen as a test case for two reasons: 1) the mean flow characteristics are very well established (being a calibration system by itself), and 2) the shear layers at the edges of the jet, especially near the exit of the nozzle, are very thin ($\sim$800-μm) with velocity gradients that are similar to those found in actuator jets. The results were compared with hot-wire measurements (being the best among all the available techniques in terms of measurement volume), as well as conventional PIV for comparison.

Test Case 2

While the first experiment was on a steady jet, the second experiment was performed on a periodic, unsteady synthetic jet. The ability to resolve small-scale coherent structures that not only have high-velocity gradients but also include the added complexity of being rotational was verified through this experiment. Both μ-PIV and conventional-PIV measurements were made on a synthetic jet actuator blowing normal to the surface. An evaluation of the capabilities of μ-PIV was achieved by looking at the minimum number of measurement points inside each rotational coherent structure.

Experiment

Based on the outcome of these two tests, μ-PIV measurements were first made to characterize the boundary layer of a flat plate with zero pressure gradient, similar to the classical experiment by Klebanoff [30]. This served as the baseline case that also helped identify 1) how close to the surface velocity measurements could be made using microscopic PIV, and 2) the ability to accurately resolve a nonlinear, high-velocity gradient boundary-layer profile.

Following this, measurements were made to characterize the synthetic jet actuator both in still air as well as in a crossflow. On the same flat plate where boundary-layer measurements were made, a voice coil-type synthetic jet actuator was flush mounted. In this case, the nozzle was modified to release the jet in the streamwise direction at an angle rather than normal as in test case 2. This is a more realistic case that has been proven to improve the flow control effectiveness of the actuator. Comparing the boundary-layer profile with the synthetic jet switched on and switched off enabled understanding the aerodynamic interaction between the jets and the boundary layer.

Table 1 summarizes the measurements and the corresponding experimental techniques.

Table 1 Measurements made in the present study

Flowfield	Technique
Steady jet (15-m/s and 50-m/s)	HWA, PIV, μ-PIV
Synthetic jet: still air (normal jet)	PIV, μ-PIV
Flat plate boundary layer	μ-PIV
Synthetic jet: still air (angled jet)	μ-PIV
Synthetic jet: crossflow	μ-PIV

Experimental Setup

A brief overview of all of the mechanical and optical systems used in the present study are provided in this section. Details of the instrumentation techniques including μ-PIV, conventional PIV, and hot-wire anemometry are also provided.

Steady Jet

The axisymmetric steady jet is provided by a calibration system (TSI, Inc. Model 1129) that is usually used to calibrate hot wires. The system includes an inlet for compressed air, a settling chamber with several honeycomb structures, a total pressure sensor at the top end of the settling chamber, and a nozzle (see Fig. 3). A feedback system sets and continuously monitors the pressure inside the settling chamber, which when contracted through the nozzle provides a jet of designated speed. The inlet of the calibrating system was modified to mix smoke with the pressurized air. The nozzle has an exit diameter of 10-mm.

Synthetic Jet

The synthetic jet actuator used in this experiment is of voice coil-type designed to fit inside a 7.5 in. chord rotor blade. The top surface of the actuator is fixed with the piston oscillating underneath. This oscillation forms a synthetic jet with a blowing and suction cycle. There is no net mass flow but net momentum is still delivered to the flow. Blowing/suction is done through a slot segmented into seven equal sections (see Fig. 4). A periodic excitation signal of type $V = V_0 \sin(\omega t)$ has been applied where V_0 is the amplitude of the excitation signal and ω is the frequency of excitation.

Boundary-Layer Measurements

Boundary-layer measurements were made in an open jet wind tunnel with circular cross section. A flat plate with rounded leading edge was placed at the exit of the nozzle section. The region of interest (ROI) in the case of μ-PIV was limited to a 10-by-10-mm plane at 0.68-m from the leading edge. The laser light sheet was focused at the center of the flat plate, and the camera with microscope was placed orthogonal to it (see Fig. 5). One thousand PIV image pairs were acquired. Freestream velocity was set at 15-m/s for all cases. This corresponds to the Reynolds number of 680,000 based on the distance from the leading edge of the flat plate to the measurement location.

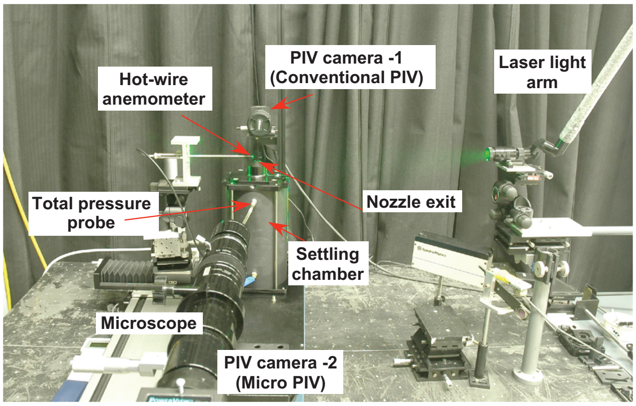

Fig. 3 Experimental setup for the steady jet measurements.

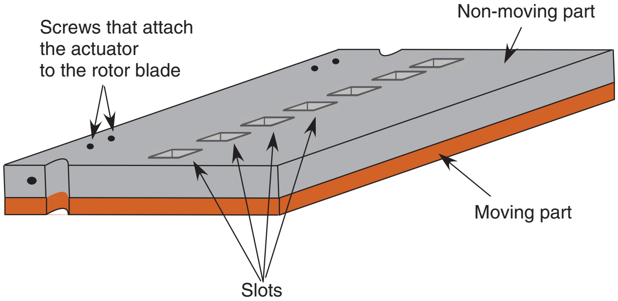

Fig. 4 Synthetic jet actuator.

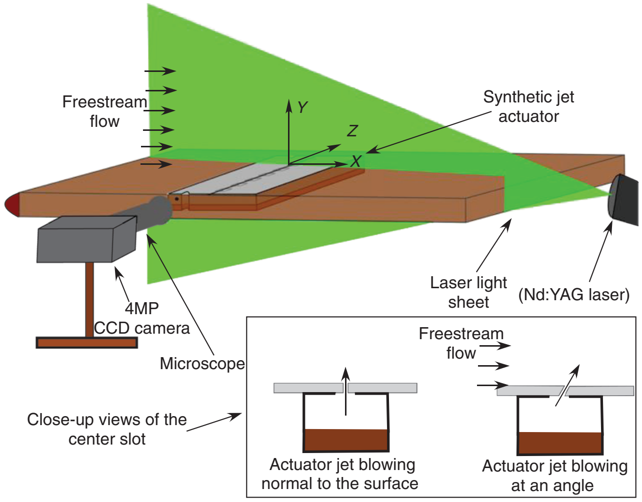

Fig. 5 Schematic of the experimental setup for flat plate boundary-layer measurements and SJA in cross flow (not drawn to scale).

Hot-Wire Anemometry

The present study used a single wire, constant temperature hot-wire anemometer that had a diameter of 3 μm. The length of the sensitive (etched) area is 1.28-mm. The distance between the two prongs is 3-mm. Overheat ratio was maintained at 1.8. Data acquisition was made at a frequency of 100-KHz, with 50-KHz low-pass filter. The time of acquisition is 0.655 s per measurement location. The probe traversed the steady jet using a high-precision traverse with an instrument precision of 0.0625-mm. The choice on the sample size and the frequency at which the measurements were conducted was estimated after performing a sweep of the frequency of acquisition and the sample size.

Microscopic PIV and Conventional PIV

For all the experiments, the light sheet was produced by a dual Nd: YAG laser, which generated a pulse (240 mJ) on the order of nanoseconds in duration at a frequency of up to 15 Hz. Two separate charge-coupled device (CCD) cameras (TSI, Inc. PowerviewPlus, model number 610039) were used for μ-PIV and conventional PIV. Both the cameras had an optical resolution of 2 K-by-2 K pixels at 12-bit resolution. Whereas one of the cameras was equipped with a microscope, the other used a conventional lens with a focal length of 105-mm. The ROI of the microscopic and conventional PIV were ~10-mm and ~50-mm, respectively.

PIV is based on the principle of estimating the displacement of seed particles in the flow. This means that the choice of seed particle plays a critical role in accurately estimating the velocity of the jet. In the present study, the seed was produced by first vaporizing a mineral oil-based fluid into a dense fog. The oil fog was then broken down into a fine mist by adding nitrogen and forced into a pressurized heater block where it was heated to its boiling point and became vaporized. As the vapor escaped from the heat exchanger nozzle, it was mixed with ambient air, rapidly cooled, and condensed into a fog. From a calibration, 95% of the particles were between 0.2-μm and 0.22-μm in diameter. The entire room was filled with this smoke before every set of image acquisition.

For steady jet measurements, the cameras for both μ-PIV and conventional PIV were placed parallel to each other, however, on either side of the laser light sheet, as shown in Fig. 3. One thousand pairs of images were acquired with each camera at each case.

In the case of synthetic jet actuators, 100 phase-locked image pairs were acquired for both microscopic and conventional PIV at every 15 deg of the actuator signal, meaning that image acquisitions were made at 24 phase locations in one cycle. Additional measurements were made at the early phases of the blowing cycle, at 5 deg resolution to better resolve the evolutionary process of the coherent structures. The pulse separation time was maintained at 1.3-μs for all the test cases and experiments. Such a low-pulse separation time has been proven to be essential to reduce measurement errors in resolving rotational flowfields [31] using PIV.

Image Processing

The acquired images were cross-correlated using a deformation grid correlation algorithm [32,33] shown in Fig. 6 combined with Rohalay Hart correlation [34]. This advanced algorithm not only employs shifting of the interrogation windows but also allows shearing in determining the velocity. This means that the velocity gradient bias errors associated with the measurements will be reduced. In the present study, the threshold signal-to-noise ratio (i.e., the ratio of first and second correlation peaks) was set at 2.0. No interpolation (or filling) was performed when an interrogation window failed the S/N condition and was not included when estimating the mean or standard deviation.

Deformation grid correlation algorithm is based on window shifting method, with a reduction in window size after every n iteration. This means that choosing the sizes of the initial and final interrogation window are critical. Whereas the size of the initial window was determined by the maximum value of the mean velocity to be measured in the flow, the final window size was determined by the velocity gradient requirements.

In the case of steady jet measurements made using μ-PIV, the initial window was as high as 48-by-48-pixels for the 50-m/s to as low as 24-by-24-pixels for the 15-m/s case. The final window size was 24-by-24-pixels in both the cases. For the unsteady synthetic jet, the size of the initial window was as high as 96-by-96-pixels and the final window size was 24-by-24-pixels, with 50% overlap.

Boundary-layer measurements were obtained by using two window sizes, 1) 24-by-24-pixels, and 2) 48-by-8-pixels, without changing their size throughout the processing. The latter (higher aspect ratio case) allowed for more velocity vectors close to the boundary, without compromising the accuracy of the correlation algorithm previously discussed.

Conventional PIV used an interrogation window size of 24-by-24-pixels all through the correlation process.

Laser Reflection

It should be understood that PIV image processing algorithms are based on correlating the intensity of the light recorded by each pixel in the camera between the two images that were acquired within a short span of time. Usually these reflections come from the moving seed particles in the flow. However, when the reflected laser light comes from a solid surface (such as in the case of a flat plate or airfoil), they tend to saturate both the images (reference and displaced). From the perspective of the processing algorithm, this basically means that the seed particles have not moved and will result in a zero displacement vector. This results in inaccurate estimation of velocity, especially near the interface between the air and solid boundary.

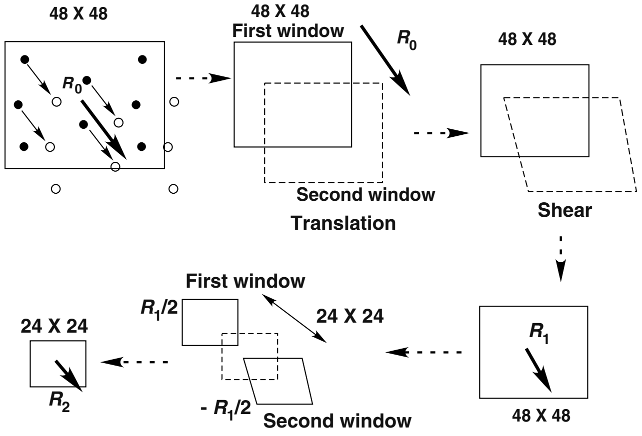

Fig. 6 Schematic explaining the deformation grid correlation algorithm.

This is a significant challenge if the goal is to make accurate boundary-layer measurements very close to the surface. Background subtraction in those situations may be challenging and time consuming [35,36]. Because this issue was expected, substantial effort has been spent to negate this during image acquisition to alleviate the challenges during image processing. In the present study, this issue was countered by various arrangements, both optically and through chemical means. First, judicious placement of the laser light sheet (by shooting along the flat plate instead of shooting normally) curbed the laser reflections significantly. Second, subtracting the background image (from all the images) that was captured before the seed particles were released into the flow helped reduce this reflection. Further reduction was possible through the application of a fluorescent dye (Kiton Red 620) on the solid surface that altered the wavelength of the incident light. By using a wavelength filter in front of the camera, it was possible to capture only the laser light and not the reflection from the surface. Any reflection that was captured after all these processes was masked so that it was not included in the correlation procedure.

Results and Discussion

The observed results will be discussed under two broad categories. First, measurements that validate μ-PIV: 1) steady jet in quiescent air and 2) unsteady, periodic synthetic jet blowing normal to the surface in quiescent air. Second, measurements made using μ-PIV to understand the interaction between the boundary layer and the synthetic jet: 1) flat plate boundary-layer measurements, 2) SJA operating in quiescent air with the jet blowing at an angle, and 3) SJA operating in crossflow.

Microscopic PIV Validation

Test Case 1: Steady Jet in Quiescent Air

This test case evaluated the capability of μ-PIV technique to accurately measure high-velocity gradients. This was achieved by comparing μ-PIV measurements with hot-wire measurements made at two different velocities across the steady jet. Comparison with conventional-PIV measurements were also made to underscore the importance of high-spatial resolution (possible only through μ-PIV technique) that is necessary to resolve the flowfield.

Initially, laser light sheet flow visualization was performed to identify the regions of aerodynamic interest, specifically those that do not introduce directional ambiguity for hot-wire measurements. Figure 7 shows the flow features of the steady jet blowing at 15 and 50-m/s obtained using laser light sheet flow visualization. It can be seen that the jet can be classified into two zones, 1) a laminar region until a particular axial distance from the nozzle exit that is free of coherent structures, and 2) a turbulent region away from the exit that is filled with several small-scale coherent structures including shedding vortex rings. The viscous nature of the fluid combined with the velocity difference between the jet and the surrounding quiescent air results in high-shear near the edges of the jet. This causes the flow to roll up as the downstream distance increases, eventually resulting in vortex rings. These flow reversal areas were avoided by keeping the μ-PIV region of focus and hot-wire measurements within one diameter of the nozzle exit. This is also where the highest velocity gradients are present, which allows a good comparison of techniques.

Figure 8a shows time-averaged velocity flowfield of the steady jet blowing at 50-m/s. Microscopic PIV measurements are shown on the left side, and conventional PIV measurements are shown on the right side. The abscissa and the ordinate are normalized by the nozzle diameter, and the velocity is normalized using the set jet velocity. The color contour represents the normalized absolute velocity $(\sqrt{U^2 + V^2})$ of the steady jet. Qualitatively, the velocity distribution looks similar in the full view between the two techniques. However, a closer look of the shear layer shown in Fig. 8b portrays a different picture. It can be seen that the μ-PIV shows a clear sharp velocity gradient that is smeared in the conventional PIV technique.

The axial velocity distribution across the jet at $x/D = 0.25$ is plotted in Fig. 9 for the hot-wire, PIV, and μ-PIV techniques. The bars spanning along the x axis at each measurement location show the size of measurement volume of each technique. In the case of hot wire, the bar is inside the symbol itself. The velocities were normalized by the corresponding set velocity of the jet in both cases. Two observations should be made here. First, until about $0.42D$ from the axis of the jet, all three techniques measured within 1% of the set velocity. Second, although the velocity of the surrounding quiescent air measured by both the PIV techniques showed almost zero velocity, hot-wire measured a higher value. This is because of the calibrating issues associated with the hot wire at very low velocities, resulting from natural convection. Nevertheless, these measurements validated the capability of both the microscopic and conventional PIV systems used in the present study to measure the mean velocity accurately, provided that the flow is uniform with negligible velocity gradient.

Although all the three measurement techniques showed a good correlation inside the steady jet, the shear layer clearly shows the differences in the capability among the measurement techniques. Microscopic PIV measurements can be seen to correlate well with the hot-wire measurements, however, with a small shift in the spatial location. The shift was found to be within one-half the size of the interrogation window. The difference in the size of the measurement volume (shown by the bars spanning along each measurement point) suggests that the dynamic range (or the velocity gradient) that was averaged within the measurement volume is significantly different between the two techniques. Despite this difference, μ-PIV can be seen to have resolved the velocity gradient within a reasonable

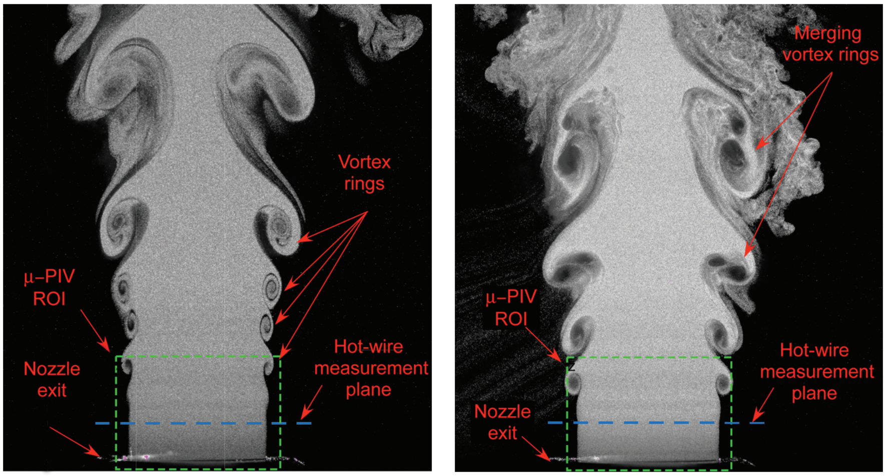

a) $U_{jet} = 15$ m/s **b)** $U_{jet} = 50$ m/s

Fig. 7 Laser light flow visualization of the steady, axisymmetric jet showing the complex nature of the flow.

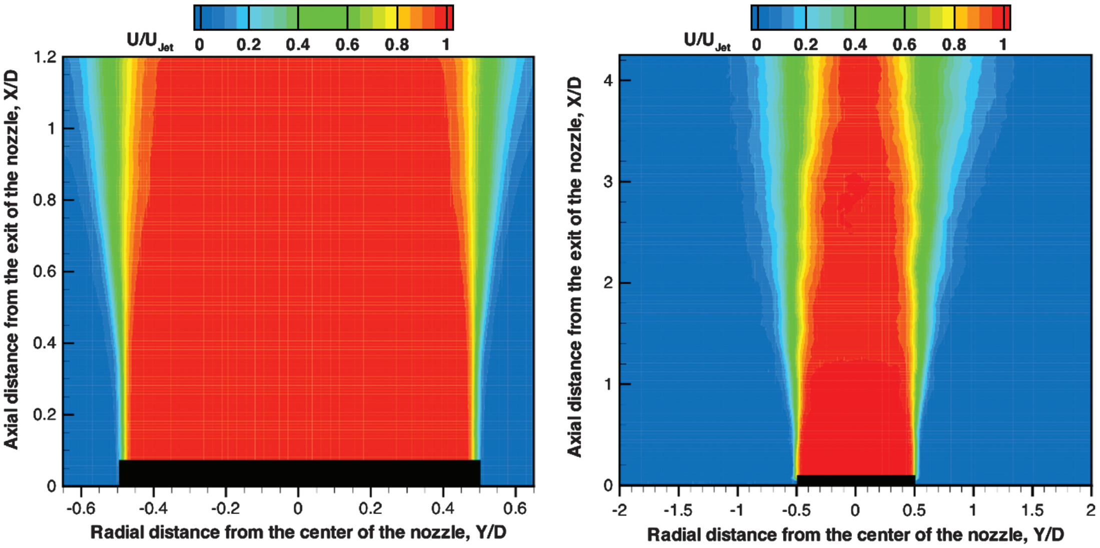

a) Full view

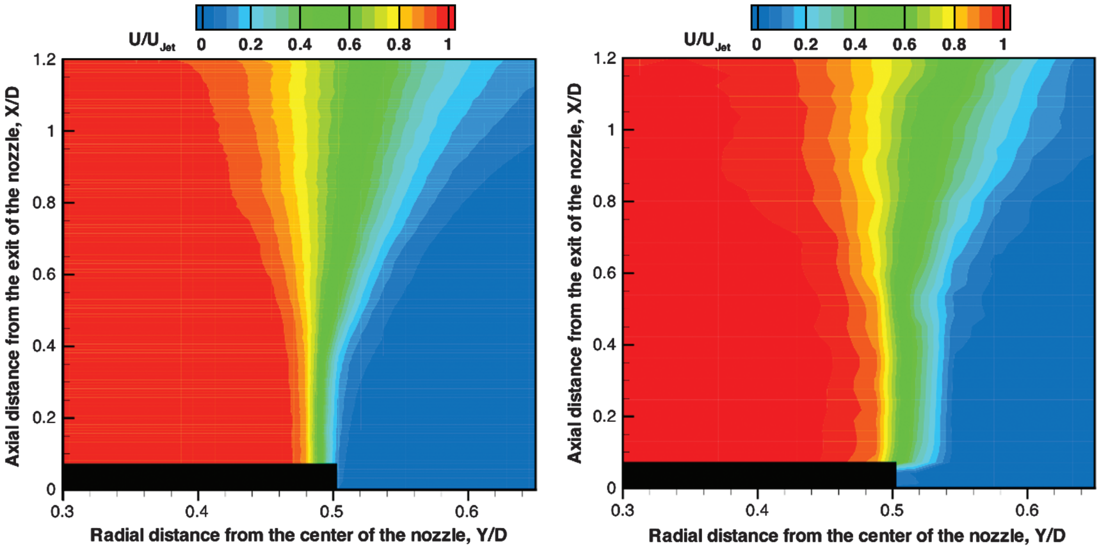

b) Close up view

Fig. 8 Steady jet in quiescent air at 50-m/s obtained using μ-PIV (left) and conventional PIV (right).

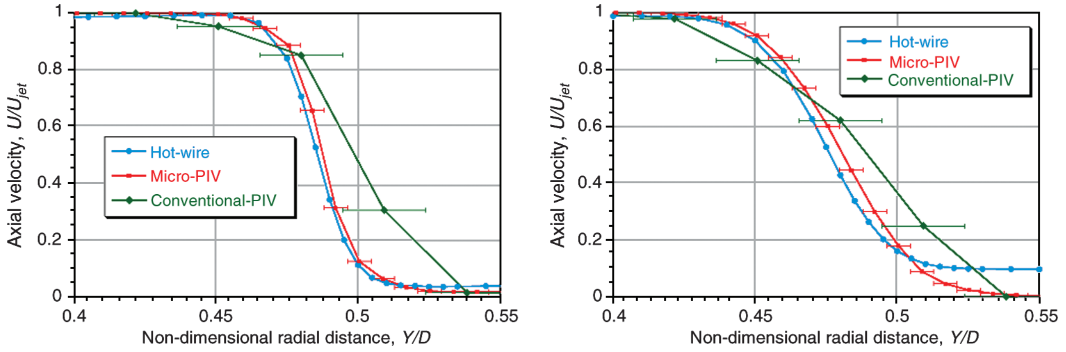

a) U_{jet} = 50-m/s

b) U_{jet} = 15-m/s

Fig. 9 Comparison of the steady jet velocity measured using various measurement techniques at $x = 0.25D$ (bars represent the size of the measurement volume of the instrumentation technique).

accuracy. This is possible only when the measurement volume (interrogation window) is small enough that the local velocity gradient (within the window) is linear. The inability of the conventional-PIV technique, on the other hand, is clearly evident in that it simply does not have the necessary resolution to resolve the high-velocity gradients. These observations conclude that μ-PIV has the necessary spatial resolution to resolve high-velocity gradients with reasonable accuracy.

Test Case 2: Unsteady Synthetic Jet in Quiescent Air

It is a well-known fact that during the blowing cycle, a synthetic jet releases a pair of counter-rotating vortices when operated in still air. The size of these vortices was of the same order as the size of the jet. This test case was performed to evaluate the capability of μ-PIV to resolve such small-scale rotational coherent structures. To achieve this, an experiment was conducted by blowing an unsteady, periodic synthetic jet in quiescent air. Microscopic PIV measurements were made using stroboscopic principle by synchronizing the laser and camera with the actuator excitation signal. Measurement using conventional PIV (lower resolution) were also made for comparison.

Figures 10a and 10b show the phase-resolved flowfield of a synthetic jet blowing normal to the surface obtained using μ-PIV at $\zeta = 15\,\text{deg}$ and $\zeta = 45\,\text{deg}$, respectively. Both the ordinate and abscissa are normalized using actuator slot width. It can be seen that the jet is symmetric about its axis. The counter-rotating coherent structures on either edges of the high-velocity jet can be clearly identified. The same measurement made using conventional PIV at $\zeta = 45\,\text{deg}$ is shown in Fig. 10c. The difference in the region of focus between the two techniques is evident. Whereas conventional PIV measured until a normal distance of 60 slot widths, μ-PIV could measure only up to 15 slot widths. A close-up view of the vortex on the right-side edge of the jet measured using both the microscopic and conventional PIV are plotted on top of each other in Fig. 10d. The black vectors show the measurements made using conventional PIV, and the red vectors show those that were made using μ-PIV. The difference in the spatial resolution between two techniques can be clearly seen. Whereas conventional PIV had five vectors inside the vortex, there are at least 25 vectors in the case of μ-PIV. This must directly translate into improved accuracy in the measurements of the jet velocity, being a high-velocity gradient flow by nature.

A radial cut made across the jet at $X/b = 3$ (through the center of both the vortices shown in Fig. 10b) is shown in Fig. 11a. The measured values of the jet and the vortices obtained using μ-PIV at this distance is consistently higher at all radial locations when compared with conventional PIV measurements. The peak velocity of the jet measured by μ-PIV was at least 20% greater than that was measured using conventional PIV. By performing uncertainty analysis on vortex measurements, Martin et al. [37] suggested that a minimum of 10 measurement points inside the vortex core are required to resolve the velocity gradients within a vortex within 1% error. It is evident that the microscopic PIV has at least 25 measurement points within the vortex satisfying this requirement.

Another radial cut made near the nozzle (slot) exit at $X/b = 0.1$ is shown in Fig. 11b. It can be seen that the peak velocity measured by conventional PIV is at least 40% lower than that measured using

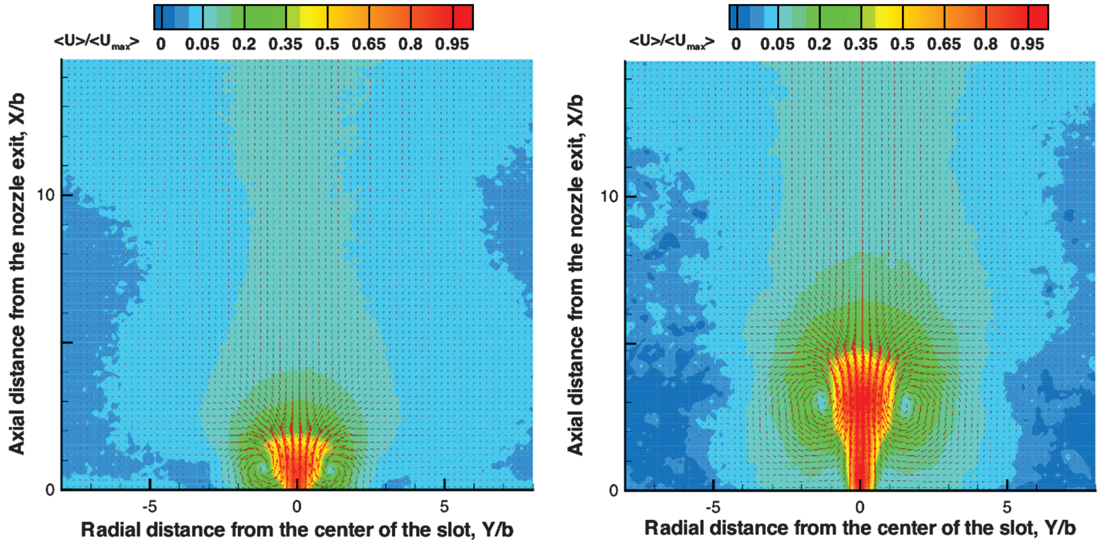

a) $\zeta = 15^{\circ}$ (Micro-PIV)

b) $\zeta = 45^{\circ}$ (Micro-PIV)

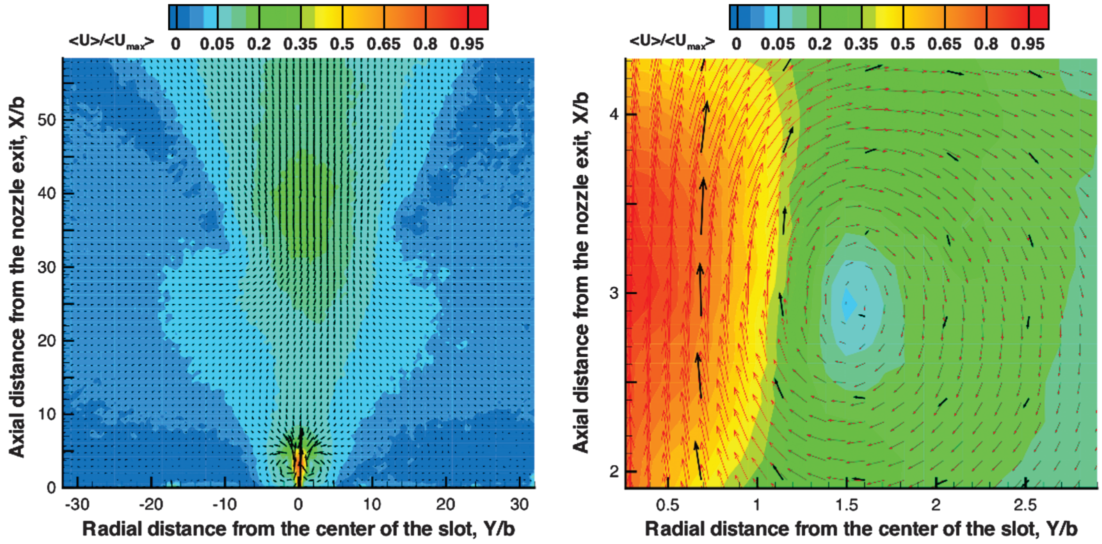

c) $\zeta = 45^{\circ}$ (Conventional-PIV)

d) Close up view; convensional-PIV (black vectors) and μ-PIV (red vectors)

Fig. 10 Flowfield of a synthetic jet actuator blowing normal to the surface in still air conditions.

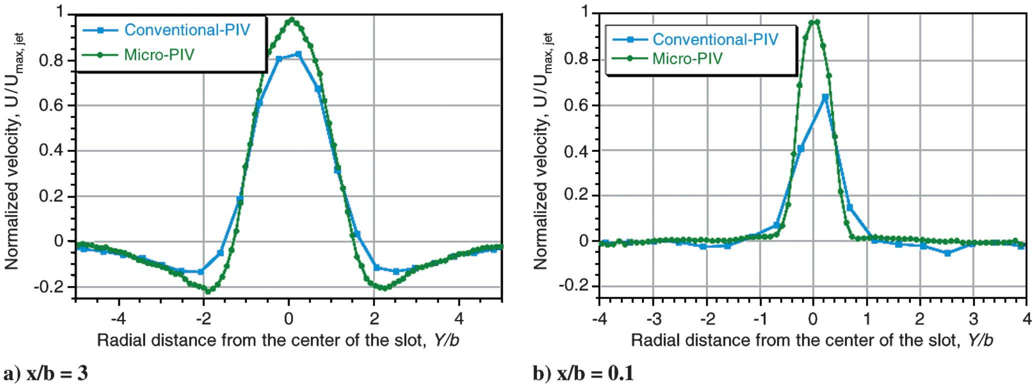

a) x/b = 3

b) x/b = 0.1

Fig. 11 Synthetic jet in still air with jet blowing normal to the exit plane.

μ-PIV. Overall, this test not only validated the capability of μ-PIV to resolve small-scale, rotational coherent structures that are found in synthetic jets, but also helped emphasize the need for high-resolution μ-PIV measurements, especially near the jet exit.

Boundary Layer And Unsteady Synthetic Jet

Having validated the capability of μ-PIV technique, the next step is to develop an experiment that will help understand the aerodynamic interaction between the synthetic jet and boundary layer. As shown in Fig. 2, this involves three independent μ-PIV measurements that include 1) flat plate boundary-layer characterization, 2) SJA operating in still air, and 3) SJA operating in crossflow. The difference between the present experiment and test case-2 in terms of the applied SJA lies in the geometry of the nozzle (slot) exit. Whereas in test case 2 the synthetic jet was blowing normal to the surface, in this experiment the slot was modified to blow the jet at an angle (52 deg) to the exit plane. Even though the μ-PIV technique has been validated, more validations were made wherever possible along the way while the observed results from the aforementioned measurements were analyzed.

Boundary-Layer Characterization

Accurately measuring the streamwise velocity distribution inside a boundary layer is a prerequisite for making measurements towards understanding the interaction between the boundary layer and synthetic jets. However, characterizing a boundary layer continues to be a challenge even though it is one of oldest problems in modern fluid mechanics. This is especially true if the goal is to measure velocities very close to the surface ($y < 100$-μm), such as inside the viscous sublayer. Very few high-fidelity measurements exists, and most of them were made using hot-wire probes specifically designed for boundary-layer measurements [38]. Optical techniques such as LDV and PIV have been used recently [39,40], but most of these measurements were made on enlarged boundary layers that were purposefully tailored to accommodate the large measurement volumes of the applied instrumentation. No measurements have been made on realistic scales that are typically found on rotors, and especially no PIV measurements exist lower than 100-μm from the surface. This is primarily because of the reflection of laser light from the surface that saturates the recorded PIV images. In the present study, significant effort has been made to reduce the reflection; the techniques that were used are explained in the experimental setup. This will serve as the baseline case to determine the effectiveness of the actuator while also evaluating the μ-PIV system in-situ.

Figure 12 shows the streamwise velocity distribution across the flat plate obtained using μ-PIV The freestream velocity was set at 15-m/s. A close-up view of the regions adjacent to the surface is shown in Fig. 12b. The thickness of the laminar boundary layer was estimated using Blasius' solution [41] given by

$$\delta_b = 4.5\sqrt{\frac{\nu}{u_0 l}} \tag{2}$$

was 3.7-mm, where ν is the viscosity of the fluid, l is the distance of the measurement location from the leading edge of the plate, and u_0 is

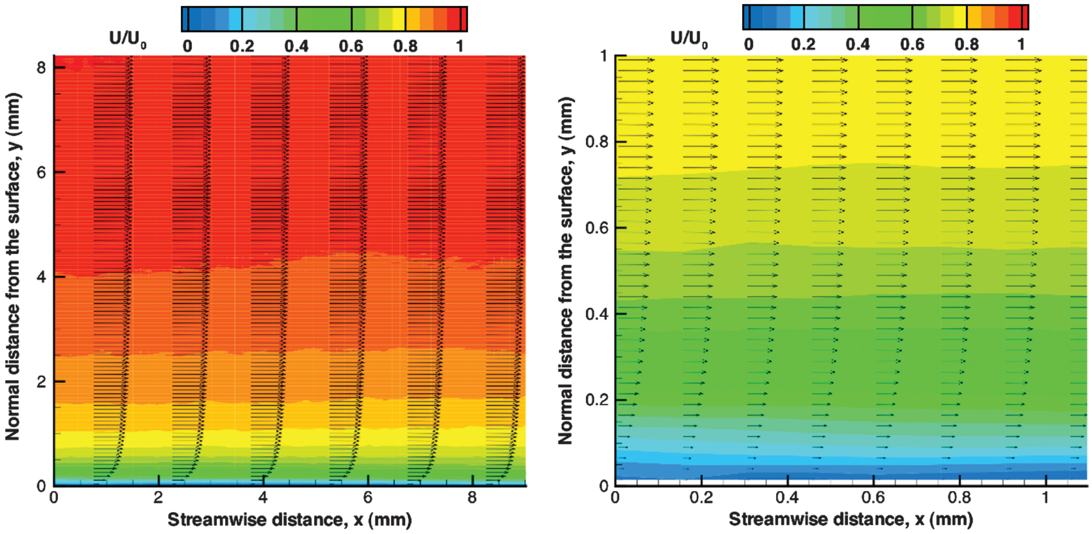

a) Full view (N=10 along the streamwise direction and N=3 along the wall normal direction)

b) Close up view (N=3 along the wall normal direction)

Fig. 12 Measured streamwise velocity on a flat plate with streamwise velocity contour.

the freestream velocity. The thickness of a turbulent boundary layer measured at the same l using

$$\delta_{\text{turb}} = 0.37l\left(\frac{\nu}{u_o l}\right)^{-0.2} \tag{3}$$

was estimated to be 17.2-mm. Because the Reynolds number at the measurement location is 680,000 (based on the distance from the leading edge of the plate to the measurement location) the flow appears to be transitional. As a result, the measured thickness of the boundary layer ($\delta \approx 7.6$-mm) lies between the laminar and the turbulent solutions.

Displacement thickness, momentum thickness, and the flux deficit inside the boundary layer were estimated at several streamwise stations using

$$\delta^* = \int_0^\infty \left(1 - \frac{u}{u_0}\right) \mathrm{d}y \tag{4}$$

$$\theta = \int_0^\infty \frac{u(y)}{u_o}\left[1 - \frac{u(y)}{u_o}\right] \mathrm{d}y \tag{5}$$

and

$$H = \rho \int_0^\infty u(y)[u_o - u(y)]\mathrm{d}y \tag{6}$$

respectively and were plotted in Fig. 13. It can be seen that within the measurement region, both the displacement and momentum thickness are relatively constant.

Figure 14 shows the measured streamwise velocity plotted against the wall normal distance (obtained at $x/b = 0$) in terms of viscous units, where

$$Y^+ = \frac{yu^*}{\nu} \tag{7}$$

and

$$U^+ = \frac{u}{u^*} \tag{8}$$

Here, u^* (friction velocity) is obtained using Clauser chart method. The law of the wall

$$U^+ = \frac{1}{\kappa}\ln(Y^+) + B \tag{9}$$

and the equation for viscous sublayer

$$U^+ = Y^+ \tag{10}$$

were also plotted along with the measurements, where κ is von Kármán constant (0.41) and B is another constant (5.5). Wall normal distances y of 100-μm and 1-mm are shown to emphasize the need for high resolution to accurately characterize the boundary layer, especially the viscous sublayer. It can be seen that the measurements follow viscous sublayer profile when $Y^+ < 5$, followed by the log law for $Y^+ > 30$. Between these two regions is the buffer layer. These excellent correlations with theory validate the capability of μ-PIV to accurately measure the velocity distribution inside the boundary layer. The accuracy of these measurements is critical considering that the effectiveness of the actuator will be based on comparison with these measurements.

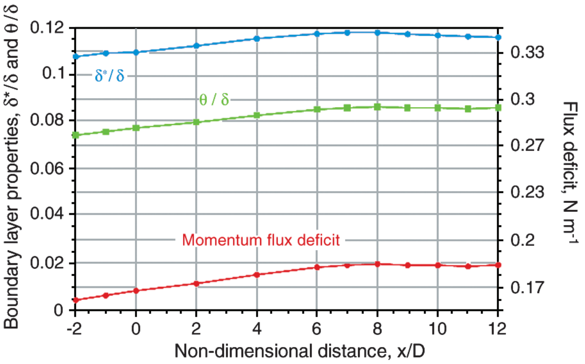

Fig. 13 Measured properties of the flat plate boundary layer.

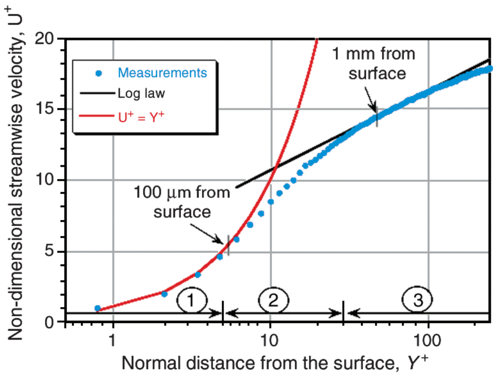

Fig. 14 μ-PIV measurements on a flat plate showing various regions of a boundary layer: 1) viscous sublayer, 2) buffer layer, and 3) log layer.

Unsteady Synthetic Jet in Still Air and in Crossflow

Figure 15 shows the peak velocity of the synthetic jet during blowing cycle (both in still air and in crossflow) measured using hot-wire anemometer and phase-resolved μ-PIV technique. The velocity values were nondimensionalized using the maximum value of velocity measured using μ-PIV when the SJA was operated in still air. The hot wire was placed at the center of the slot exit to prevent any ambiguity in the direction of flow caused by the presence of lip vortices. An excellent correlation exists between the two measurement techniques, further validating μ-PIV measurements. An interesting observation here is that the measured velocity of the jet is not smooth (or sinusoidal) as the blowing cycle progresses. It can be seen that the measured velocity of the jet begins to increase rapidly as the blowing cycle starts ($0\,\text{deg} \le \zeta \le 15\,\text{deg}$). This was followed by shallow increases to the peak value between $\zeta = 15\,\text{deg}$ and $\zeta = 90\,\text{deg}$, with the peak occurring at $\zeta = 90\,\text{deg}$. The reduction in the slope has been associated with the formation of secondary vortices [8]. As the blowing cycle progresses, the measured velocity reduces smoothly before the suction cycle starts. In the case of SJA operating in crossflow, the measured velocity shows higher value at all phases because of the additional freestream velocity included in all the vectors.

Mass and Momentum

Figure 16 shows the mass flow rate and momentum through the nozzle of the SJA. Whereas mass flow rate was obtained by integrating the normal velocity across the slot width, momentum was

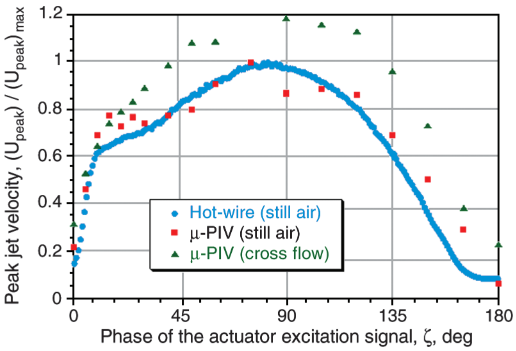

Fig. 15 Comparison of phase-resolved peak blowing velocity measured using hot-wire and μ-PIV.

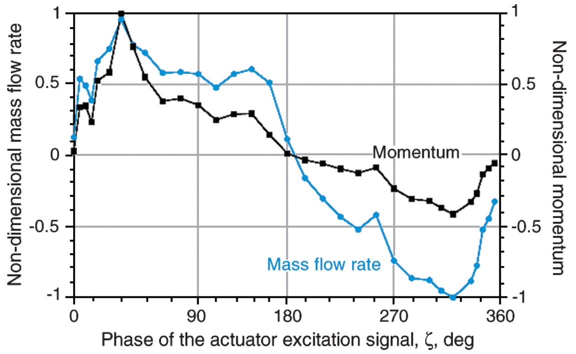

Fig. 16 Characteristics of the synthetic jet actuator measured in crossflow.

estimated from the product of mass and the absolute velocity. The values were nondimensionalized using the corresponding peak values. It can be seen that the total mass inflow into the SJA during the suction cycle equals the total mass outflow during the blowing cycle, resulting in zero net mass flow, as expected for an SJA. However, the net momentum added to the flow can be seen to be positive.

Blowing Cycle

Figures 17–19 show the phase-averaged μ-PIV measurements acquired during various phases of the blowing cycle of the SJA operating in still air (left) and in crossflow (right). The distances in both cases were normalized using the measured flat plate boundary-layer thickness. In the case of the synthetic jet operating in still air, this allowed estimating the probable depth of penetration of the jet into the boundary layer under ideal conditions (i.e., without any aerodynamic interaction between synthetic jet and boundary layer). Also, in both these cases the color contour represents the streamwise velocity normalized by the freestream velocity.

Explaining the formation and evolution of the lip vortices, to begin with, is logical considering the role they play in the momentum transport. Figure 17a (left side) shows the velocity contour of the flowfield when the SJA was operated in still air with the jet blowing at an angle. This portrays a different picture from what was expected based on test case 2 in that these vortex pairs did not form simultaneously on either edge of the jet. While the left-side vortex can be seen at $\zeta = 5$ deg, the roll up on the right-side edge of the jet occurred with a phase delay ($\zeta = 10$ deg). Because the nozzle exit is placed at an angle, the right-side edge of the jet is close to the surface and the left-side edge is away from it. The mere presence of a solid boundary near the right edge of the jet seems to play a role in the delayed roll up of the lip vortex, suggesting that the development of the jet may not be symmetrical.

On the other hand, in the case of SJA operating in crossflow, there is only one vortex and it forms on the right side of the jet. Although the lip vortices on either edge of the jet can be clearly identified in the case of SJA operating in still air, only the right-side edge of the jet has rolled up into a vortex when the SJA was operated in crossflow. This is because of the direction of the freestream flow that opposes the roll up on the left side. Also, the measured peak swirl velocity of the left lip vortex (in still air case) is approximately the same magnitude as the freestream velocity in crossflow, but with a negative sign. This suggests that this may be a special case where the swirl velocity of the vortex is of the same order as that of the freestream velocity, preventing the roll up on the left side.

A higher jet velocity (and the associated increased peak swirl velocity of the lip vortex) may provide different results, in that both the left and right vortices may form. It should, however, be noted that in the present study the velocity of the jet is at least four times higher than the freestream velocity. Even though such a ratio is desirable, current status of SJA is such that the jet velocity is lower than the freestream velocity, meaning that the left-side lip vortex will not form in crossflow.

For description purposes, the left-side vortex will henceforth be referred to as the windward-side vortex, as the flow is from left to right. The right-side vortex is referred as lee-side vortex. These notations are followed both in the still air case and in the crossflow case.

The evolution of the lip vortices were also found to be different in still air and in crossflow. In the still air case, both the windward-side and the lee-side vortices convect away from the actuator surface and also away from each other (see Figs. 17b, 17c, and 18a–18c). The lip vortices play a significant role in transferring the momentum from the jet to a wider region in the flow. The windward-side vortex can be seen to travel as high as the outer layer of the boundary layer (or even higher). As both the vortices convect through the quiescent air, the strength of the vortices continue to decrease because of viscous diffusion. Eventually, these lip vortices become part of the jet itself.

In the case of SJA operating in crossflow, an immediate consequence of the absence of the windward-side vortex appears in the orientation of the jet downstream of the slot exit. Whereas the synthetic jet operating in still air maintains its orientation (same as the inclination of the nozzle), the synthetic jet operating in crossflow aligns itself almost parallel to the freestream velocity within a very short distance downstream from the nozzle exit. In the latter case, the change in orientation results from 1) the presence of the crossflow, and 2) the presence of just the lee-side vortex and its associated induced velocity (without any countereffect from the windward-side vortex) that pulled the jet toward the solid surface.

Figure 20 shows the trajectory of the jet obtained by tracking the peak value of velocity along the streamwise direction. The figure also includes the trajectory expected from an inclined, axisymmetric steady jet given by Wu [42] that was corrected for synthetic jet applications by Eroglu and Breidenthal [7], given by

$$\frac{y}{\mathrm{VR}b} = 1.75\left(\frac{x}{\mathrm{VR}b}\right)^{0.38} \tag{11}$$

This plot basically shows the difference in the trajectory between an axisymmetric synthetic jet (with a circular nozzle) and an asymmetric plane jet (such as the one in the present study, where only the lee-side vortex is present). The substantial reduction in the depth of penetration clearly shows how a boundary layer interacts differently between a symmetric and an asymmetric jet. This means that more momentum will be added closer to the wall in the asymmetric case than in the symmetric case, a beneficial factor. However, interaction with the outer layer or with the mean flow to bring energy into the boundary layer becomes questionable.

This increased inclination of the jet, in turn, has another important consequence. It can be seen that the solid surface acts as a boundary on one side of the vortex and the jet forms the boundary on the other side, trapping the vortex between the jet and the solid surface. It is very well known that the presence of a solid surface resists any motion in a viscous fluid (no slip condition), whether it is upstream or downstream. As a result, the vortex faces significant resistance in maintaining its coherence. However, the vortex continues to get energy from the jet as the blowing cycle continues. These two actions compete against each other, eventually resulting in the breakdown of the vortex. The remnants of the vortex can be seen in Figs. 18b, 18c, 19a, and 19b. The process leading to the breakdown of the lee-side vortex can be expected to reduce the momentum that should have otherwise been added to the boundary layer, resulting in reducing the efficiency of the system.

Increasing the inclination of the nozzle by allowing the jet to shoot more normally (away from the surface) might be beneficial in that it will increase the depth of penetration of the jet deep into the outer layer of the boundary layer, and also by not trapping the vortex. Increasing the penetration of the jet will be beneficial in terms of bringing the energy from the mean flow into the boundary layer. Also, in real applications when the SJA is used to prevent flow separation, most often the SJA slot exit is placed at the quarter-chord of the airfoil (or the point of the maximum thickness). This means that the angle between the jet and the surface downstream of the slot automatically increases, a favorable condition that may prevent the breakdown of the vortex, resulting in a better transport of momentum. Optimizing the inclination of the jet with respect to the

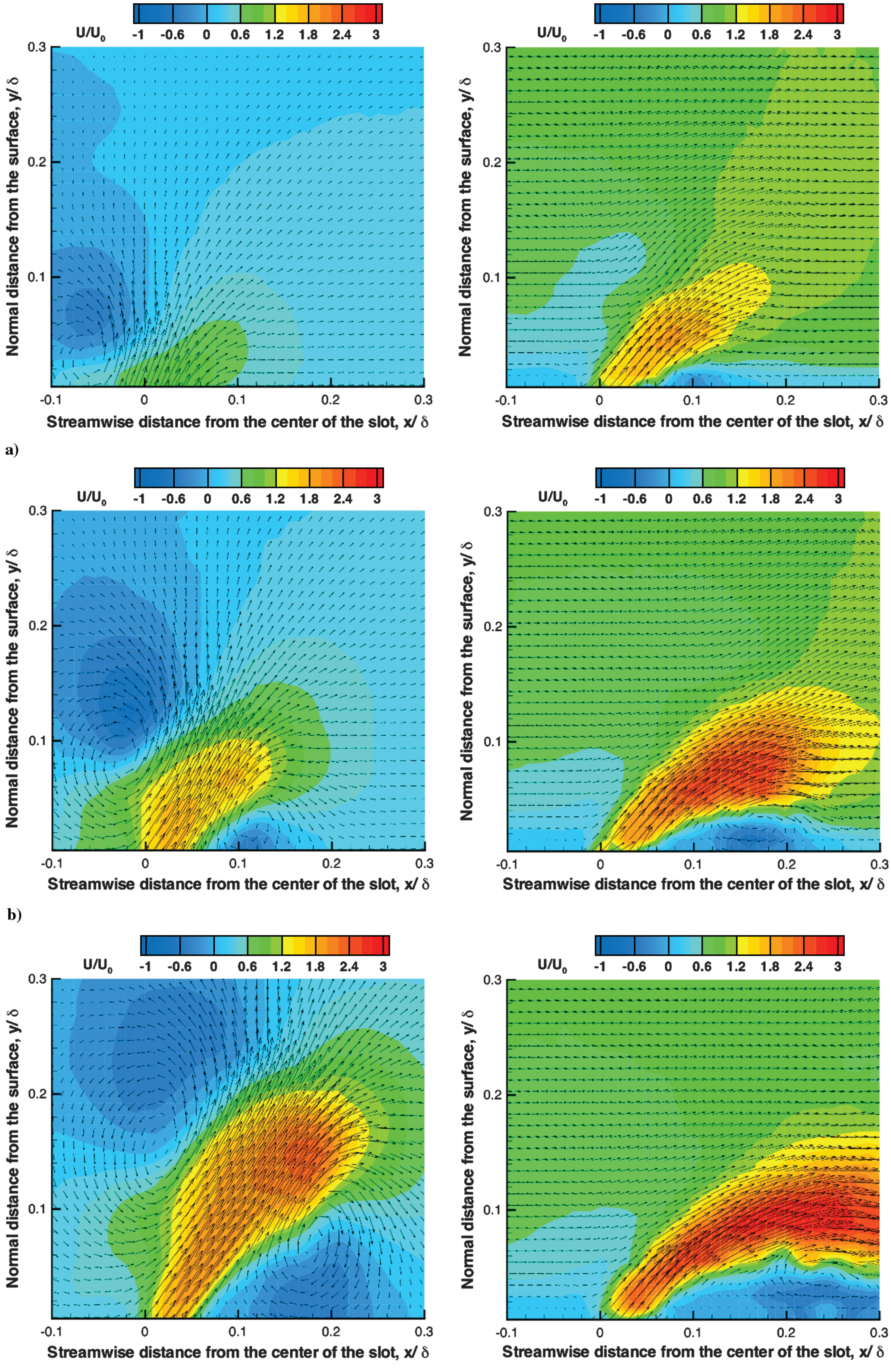

a)

b)

c)

Fig. 17 Velocity contour of the phase-averaged μ-PIV measurements made on an unsteady SJA during blowing cycle, in quiescent air (left) and in crossflow (right): a) $\zeta = 5\,\mathrm{deg}$, b) $\zeta = 10\,\mathrm{deg}$, and c) $\zeta = 15\,\mathrm{deg}$.

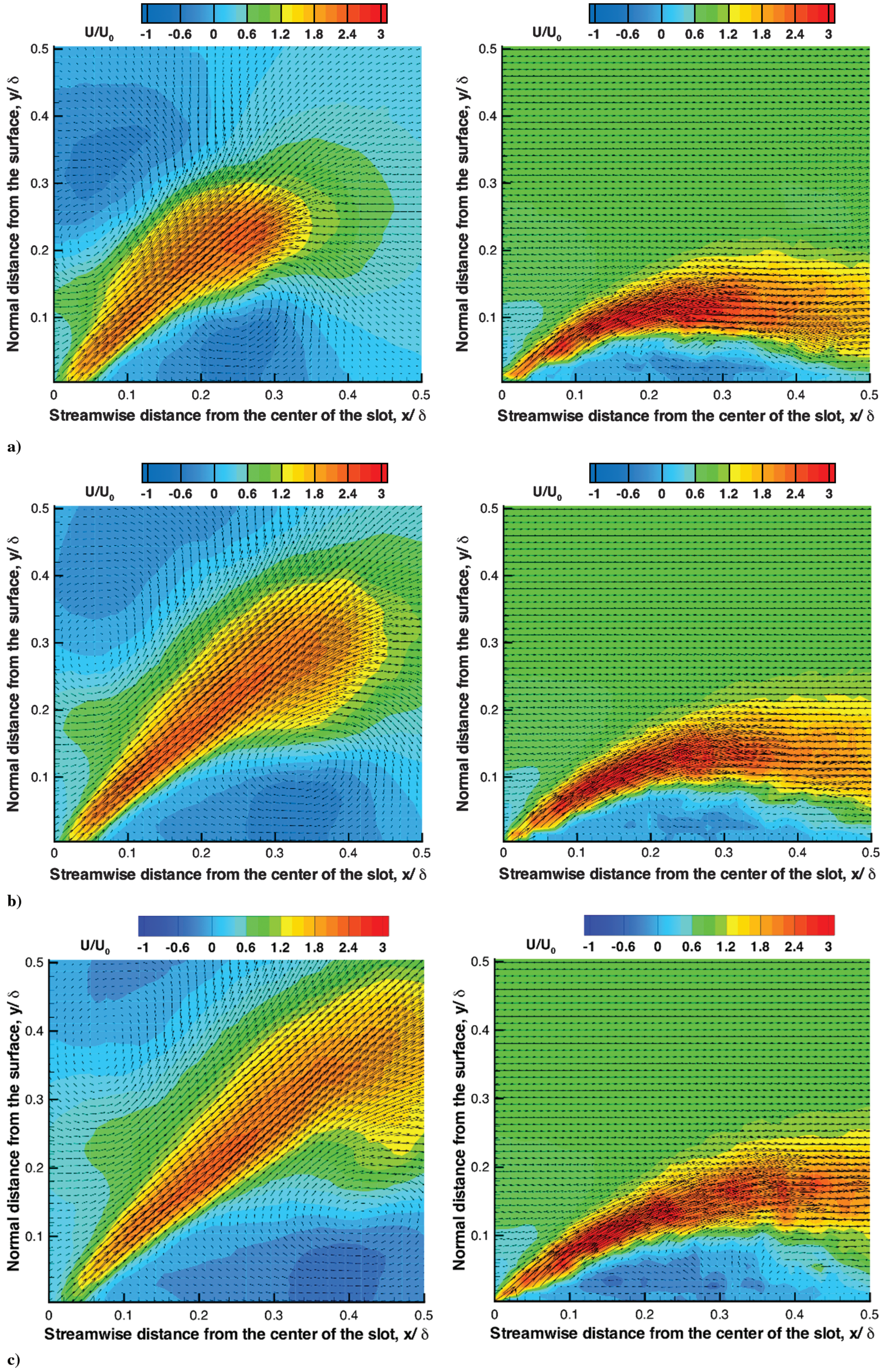

Fig. 18 Velocity contour of the phase-averaged μ-PIV measurements made on an unsteady SJA during blowing cycle, in quiescent air (left) and in crossflow (right): a) $\zeta = 20\,\mathrm{deg}$, b) $\zeta = 25\,\mathrm{deg}$, and c) $\zeta = 30\,\mathrm{deg}$.

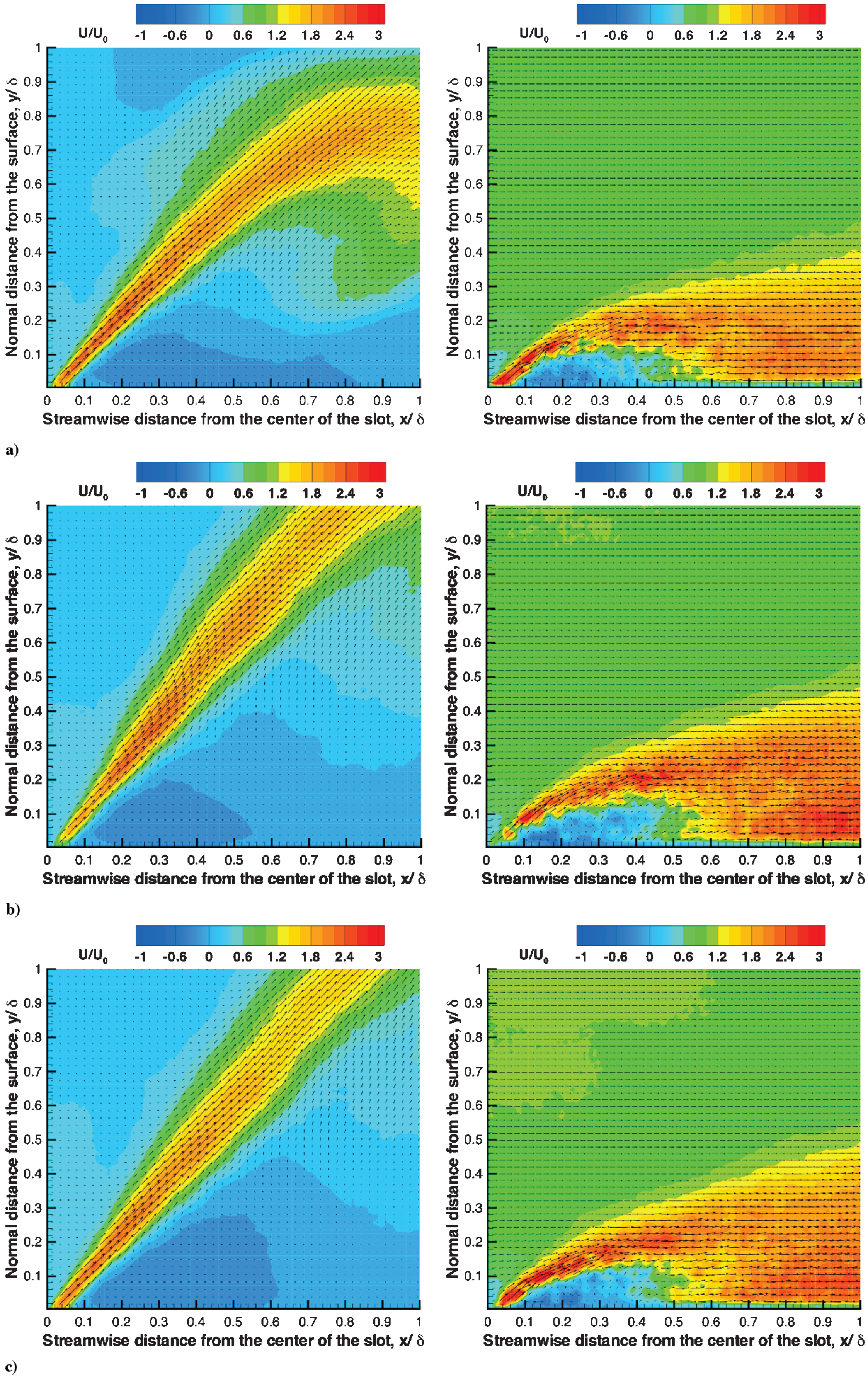

Fig. 19 Velocity contour of the phase-averaged μ-PIV measurements made on an unsteady SJA during blowing cycle, in quiescent air (left) and in crossflow (right): a) $\zeta = 60\,\mathrm{deg}$, b) $\zeta = 90\,\mathrm{deg}$, and c) $\zeta = 120\,\mathrm{deg}$.

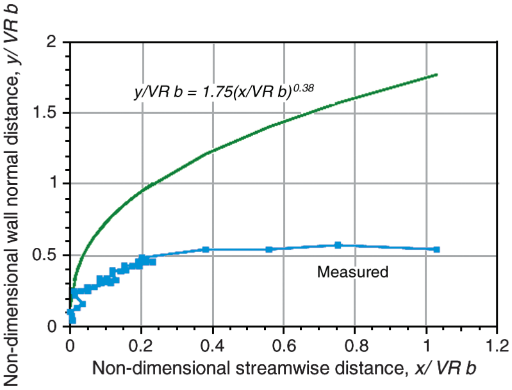

Fig. 20 Measured and expected trajectory of the synthetic jet in crossflow.

exit plane appears to be a key parameter in improving the flow control effectiveness of actuators, and is an area of future research.

Flow Reversal

Figures 19b and 19c show the full flowfield measured by μ-PIV. Synthetic jet induces the surrounding flow to align with its axis, especially at its edges. In the case of the synthetic jet operating in still air, the entire flowfield can be divided into two zones, separated by the axis of the jet (or at the diagonal of the image). On the upper half (upstream edge of the jet) the horizontal component of velocity can be seen to be positive and upward. However, in the lower half the horizontal component of velocity is negative (i.e., the flow is in the upstream direction). This is especially evident close to the surface (relatively large zone with dark blue color contour).

The effect of the induced velocity of the jet on the surrounding flow is similar in crossflow as well. This means that the area between the jet and the solid surface experiences flow reversal (negative streamwise velocity). Also, the direction of rotation of the lip vortices (before they break down) aids flow reversal closer to the surface. As a result, almost throughout the entire blowing cycle a small region

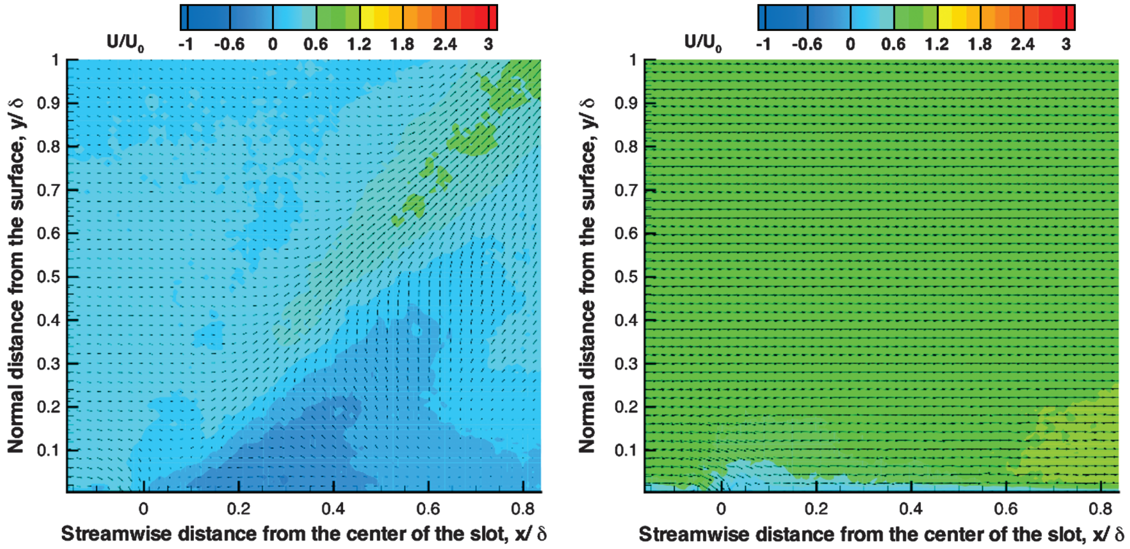

a) $\zeta = 180°$

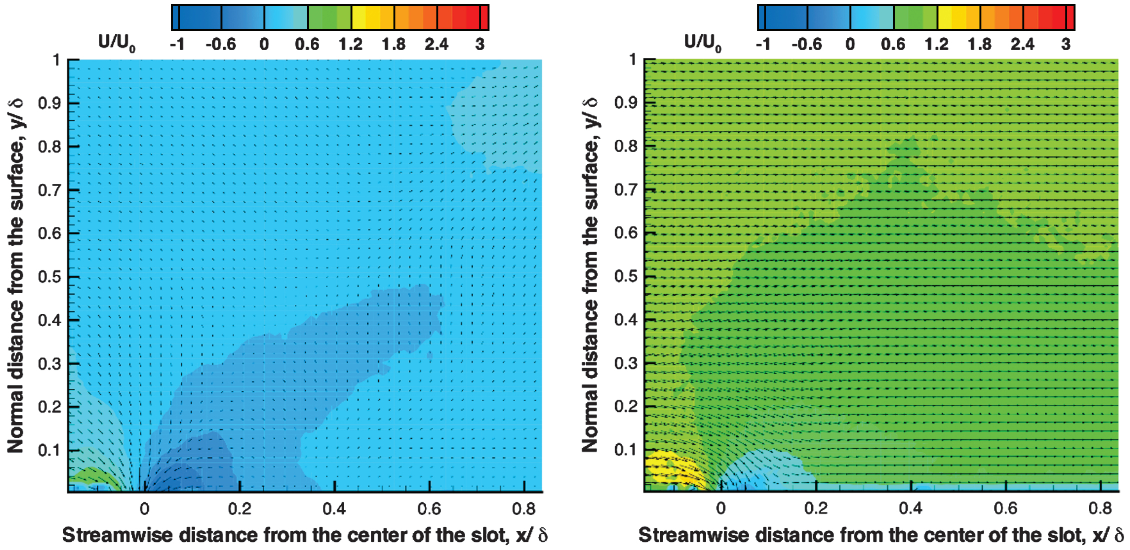

b) $\zeta = 240°$

Fig. 21 Velocity contour of the phase-averaged μ-PIV measurements made on an unsteady SJA during suction cycle in quiescent air (left) and in crossflow (right).

downstream of the slot exit will always remain opposite to that of the streamwise direction (shown by the blue color contour). As the streamwise distance from the slot exit increases ($x/\delta > 0.5$), the streamwise velocity becomes positive because of the direct addition of momentum from the jet. The region between the nozzle exit and $x/\delta > 0.4$ appears like a separation bubble with low recirculation. By about one boundary layer thickness downstream from the slot exit, the flow can be seen to be uniform and free of any coherent structure.

Suction Cycle

Figure 21 shows the phase-averaged flowfield during the suction cycle of the synthetic jet actuator both in still air (left) and in crossflow (right). In the case of SJA operating in still air, the stagnation point can be easily located. No coherent structure can be seen. As the suction cycle progresses, more and more region was influenced by the suction pressure of the actuator. Also, the magnitude of suction velocity was found to increase.

Figure 22 shows the streamwise velocity distribution along the wall normal direction at 12 slot widths downstream of the slot exit (approximately at one boundary layer thickness) throughout the entire SJA cycle. The phase locations marked on top of the profiles correspond to the phase of the SJA excitation signal. Because the cut is made far downstream of the slot exit, it can be seen that it takes approximately 45 deg in terms of the actuator cycle time for the effect of jet to be felt. At about 135 deg, which corresponds to the 90 deg of the SJA signal, it can be seen that the depth of penetration reaches maximum value. The phase-averaged velocity values are more than twice the freestream velocity, suggesting significant addition of momentum. As the blowing cycle completes, it can be seen that the velocity profiles go back to their original condition at around 210 deg. The effect of the suction pressure of the actuator was not felt this far downstream.

Region of Influence

Time-averaged velocities that are obtained by averaging all the phase-average velocities are shown in Fig. 23. It can be seen that the influence of synthetic jet in still air reaches up to a normal distance equivalent to the outer edge of the boundary layer. However, in the case of crossflow, not more than 60% of the boundary layer was affected by the synthetic jet. This is despite having the jet velocity four times higher than the freestream velocity. This means that the momentum added to the boundary layer is only through the momentum from the SJA.

Figure 24a shows the streamwise velocity distribution along the wall normal direction (at various streamwise stations) obtained from the time-averaged μ-PIV measurements made on the SJA operating in crossflow. The streamwise velocity distribution from the simple, flat plate boundary layer is also included for comparison. Two slot widths upstream of the slot exit it can be seen that the streamwise velocity is higher at all locations compared with the simple boundary-layer measurements. This is primarily because of the additional momentum added to the flow during suction cycle, where the low pressure created by the SJA actuator accelerated the flow. At two slot widths downstream from the slot exit the jet is confined

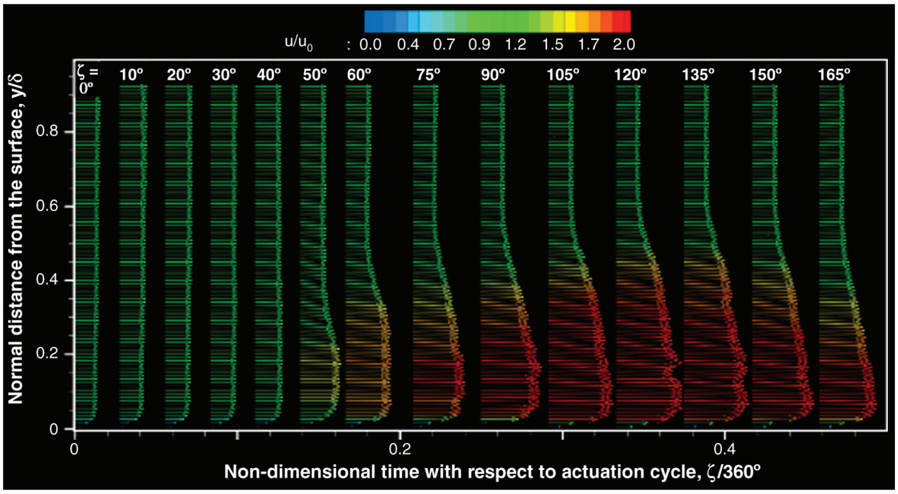

a) Blowing cycle

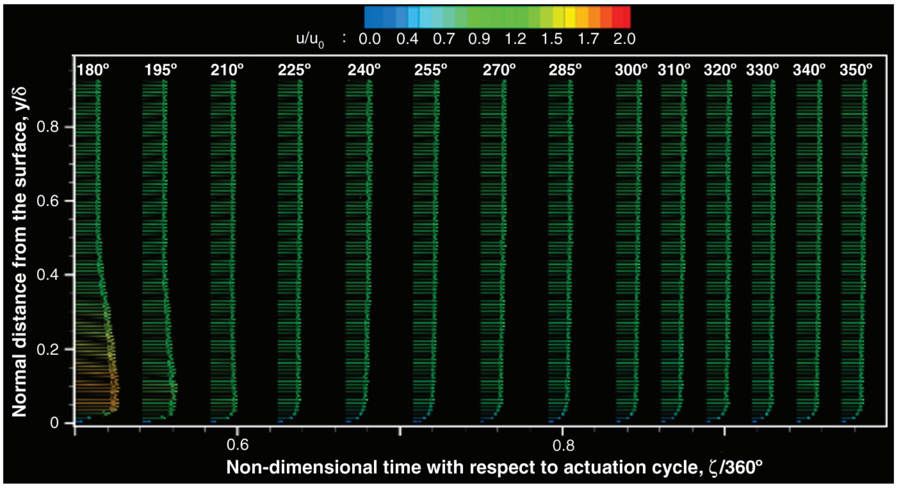

b) Suction cycle

Fig. 22 Phase-averaged μ-PIV measurements at $x/b = 12$ throughout the entire SJA cycle.

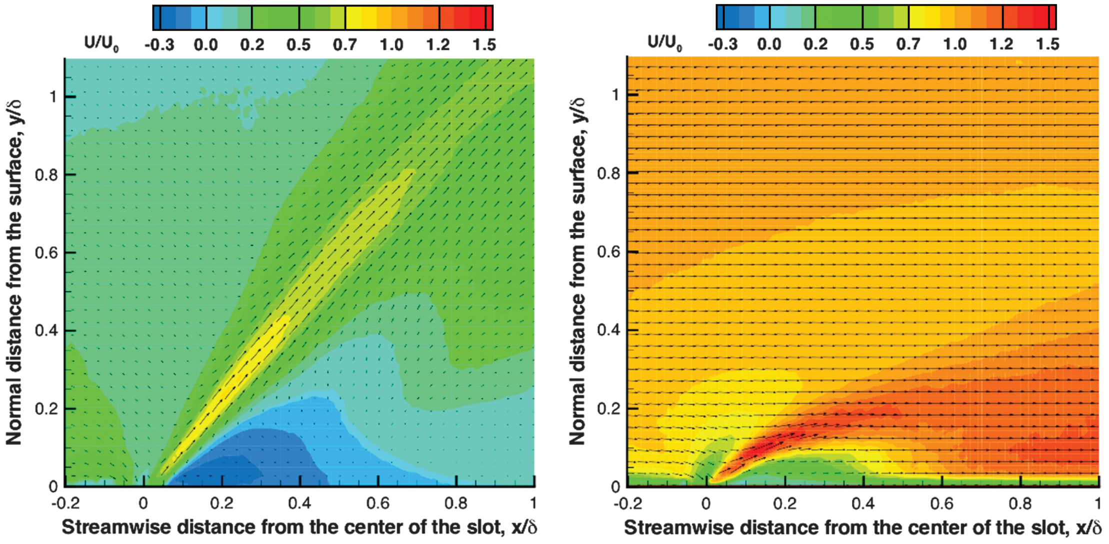

a) Unsteady synthetic jet in quiescent air **b) Unsteady synthetic jet in cross flow**

Fig. 23 Time-averaged μ-PIV measurements

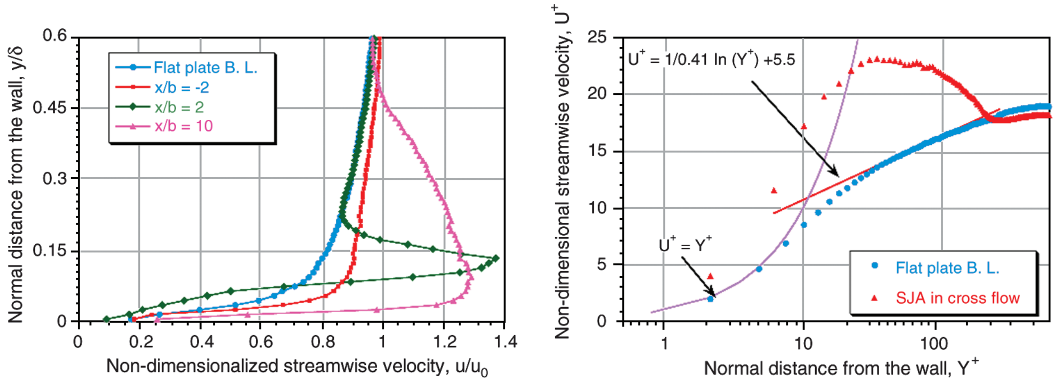

a) At various downstream distances **b) In terms of viscous units**

Fig. 24 Comparison of time-averaged streamwise velocity profiles between a simple boundary layer and when the synthetic jet was operated in crossflow.

within a small region. As a result, it can be seen that the streamwise velocity is almost twice that found in simple boundary-layer measurements. Very close to the surface, however, the velocity is lower than that was measured on the simple flat plate boundary layer, indicating the presence of upstream flow (negative streamwise velocity) reducing the overall average. The region of influence of the jet can be seen to increase continuously as downstream distance increases, to reach as high as 60% of the boundary layer from the surface at about 10 slot widths downstream from the slot. Figure 24b shows the velocity distribution normal to the wall in terms of viscous units. All the momentum that is added to the flow by the SJA can be seen to alter the viscous sublayer and the log layer. The outer layer seems unaltered, clearly suggesting that there is no interaction with the mean flow.

Figure 25a shows the momentum thickness obtained from the time-averaged boundary-layer measurements at various downstream distances when the SJA was operated in crossflow using Eq. (5). The associated momentum flux deficit estimated using Eq. (6) is shown in Fig. 25b. As expected, both the figures show the same trend. Both these figures also include measurements obtained by vectorial addition of the flow over simple flat plate and synthetic jet operating in still air (an ideal case). In all these cases, the measured values were normalized using the corresponding values from simple flat plate boundary-layer measurements.

Momentum thickness can be defined as the distance the solid boundary should be moved to compensate for the reduction in momentum caused by the presence of boundary layer. At the jet exit $x/D = 0$ the momentum thickness of simple flat plate boundary layer and that of a synthetic jet operating in crossflow are almost the same. This is because the time-averaged incoming and outgoing velocity from the nozzle exit is zero, causing no change in the momentum thickness. On the other hand, slightly upstream of the nozzle exit, it can be seen that the momentum thickness of the SJA in crossflow case shows lower momentum thickness. This means that the momentum lost inside the boundary layer has reduced. The only source for this to happen comes during the suction cycle when the SJA draws in air from all directions. This accelerates (adds the momentum) to the flow causing a reduction in the momentum flux deficit.

The momentum thickness and the momentum flux deficit continue to decrease with increasing distance from the SJA nozzle exit. This, however, is expected and is from the direct addition of momentum from the SJA. An interesting observation is that the momentum thickness becomes negative, suggesting that the momentum added to the boundary layer completely removed the momentum lost because of the formation of the boundary layer. To maintain the same momentum as that of the potential flow, the solid boundary must be moved down. It is also clear that the ideal case (where the simple boundary-layer velocity profile was vectorially added to the SJA flow in still air) shows the exact same behavior as the real SJA in crossflow except that the momentum added to the fluid is significantly higher than that observed in real crossflow conditions. This clearly suggests

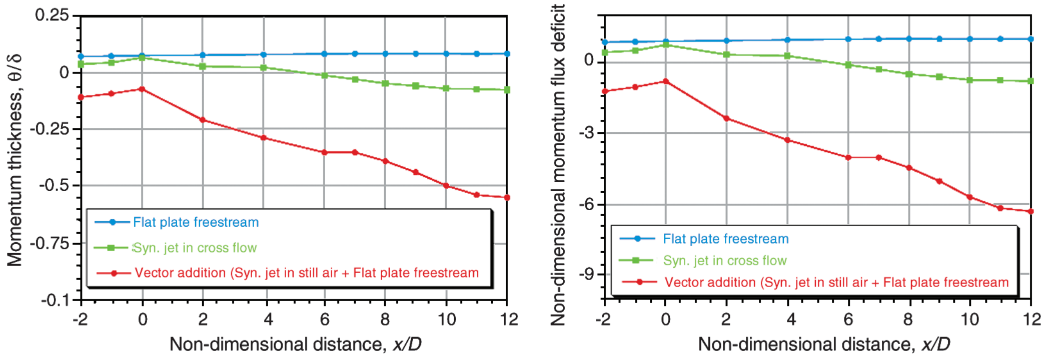

a) Momentum thickness

b) Flux deficit

Fig. 25 Measured properties of the boundary layer showing the effectiveness of the SJA.

that the aerodynamic interaction between the synthetic jet and the boundary layer unfavorably affects the performance of the actuator.

Conclusions

Microscopic PIV measurements were made toward understanding the aerodynamic interaction between an unsteady, inclined synthetic jet and a boundary layer in a building block approach. Emphasis was made to ensure that the μ-PIV technique has the ability to resolve all the complex flow features such as high-velocity gradient flowfield, small-scale coherent structures, and so forth, that are essential to understand this interaction.

The following are specific conclusions derived from the present study:

1) The spatial resolution provided by μ-PIV seems to be necessary (and sufficient) for resolving the physical dimension of the synthetic jet, its high-velocity gradient, and the associated small-scale rotational coherent structures. Comparison with hot-wire measurements showed excellent correlation, validating the μ-PIV technique. Conventional PIV, on the other hand, was found to have insufficient spatial resolution to perform this study.

2) The synthetic jet was found to add momentum to the boundary layer without any addition of mass, as expected. This was verified by the reduced momentum flux deficit and the associated reduction in momentum thickness. However, all of the addition of momentum had its source from the synthetic jet actuator itself. The jet never reached beyond 60% of the boundary-layer thickness from the surface to interact with or transport energy from the mean flow. All of the interaction caused by the synthetic jet was limited to the viscous sublayer and log layer.

3) The time evolution of the synthetic jet in still air and in crossflow were almost completely different. The results suggested that any performance prediction, such as momentum added to the boundary layer or the penetration of the jet in terms of boundary-layer thickness based on still air conditions may not be applicable in crossflow conditions at all. The aerodynamic interaction between the synthetic jet and boundary layer was found to unfavorably alter the effectiveness of the actuator.

4) μ-PIV technique has the necessary spatial resolution to resolve the nonlinear velocity gradients found near the wall in a boundary layer. The issues of laser reflection were successfully mitigated, which allowed velocity measurements to be made as close as 20μm to the surface. The present measurements met the test objectives, clearly establishing the bounds for critical parameters to apply μ-PIV for the forthcoming dynamic stall control experiment.

Acknowledgments

The authors gratefully acknowledge the discussions with M. S. Chandrasekhara and Mahendra J. Bhagwat, which were helpful throughout the work. Our appreciation extends also to Robert Ormiston, Frank Caradonna, and Chee Tung for reviewing the paper and providing valuable suggestions. The support and cooperation of Hank Schwoob, Gary Buob, Bruce Gesek, Brian Chan, Jon Lautenschlager, Bruce Stroms, and Steve Nance were greatly appreciated.

References

[1] Landgrebe, A. J., "The Wake Geometry of a Hovering Rotor and its Influence on Rotor Performance," *Journal of the American Helicopter Society*, Vol. 17, No. 3, Oct. 1972, pp. 3–15.

[2] Egolf, T. A., and Landgrebe, A. J., "Helicopter Rotor Wake Geometry and its Influence in Forward Flight, Vol. 1: Generalized Wake Geometry and Wake Effects in Rotor Airloads and Performance," NASA, Rept. CR-3726, Oct. 1983.

[3] Caradonna, F., Hendley, E., Silva, M., Huang, S., Komerath, N., Reddy, U., Mahalingam, R., Funk, R., Wong, O., Ames, R., Darden, L., Villareal, L., and Gregory, J., "Performance Measurement and Wake Characteristics of a Model Rotor in Axial Flight," *Journal of the American Helicopter Society*, Vol. 44, No. 2, 1999, pp. 101–108. doi:10.4050/JAHS.44.101;

[4] Ramasamy, M., Johnson, B., and Leishman, J. G., "Understanding the Aerodynamic Efficiency of a Hovering Micro-Rotor," *Journal of the American Helicopter Society*, Vol. 53, No. 3Oct. 2008, pp. 412–428.

[5] Martin, P. B., Tung, C., and Chandrasekhara, M. S., "Active Separation Control Measurements and Computations for a NACA 0036 Airfoil," *Proceedings of the 21st AIAA Applied Aerodynamics Conference*, 2003-3156, AIAA, Reston, VA, June 23–26 2003.

[6] Martin, P. B., Wilson, J. S., Berry, J. D., Wong, T., Moulton, M., and McVeigh, M. A., "Passive Control of Compressible Dynamic Stall," *Proceedings of the AIAA 26th Applied Aerodynamics Conference*, 2008–7506, AIAA, Reston, VA, Aug. 18–21 2008.

[7] Eroglu, A., and Breidenthal, R. E., "Structure, Penetration, and Mixing of Pulsed Jets in Crossflow," *AIAA Journal*, Vol. 39, No. 3, March 2001, pp. 417–423.
doi:10.2514/2.1351

[8] Wu, J. M., Vakili, A. D., and Yu, F. M., "Investigation of the Interacting Flow of Nonsymmetric Jets in Crossflow," *AIAA Journal*, Vol. 26, No. 8, Aug. 1988, pp. 940–947.
doi:10.2514/3.9994

[9] Greenblatt, D., and Wygnanski, I., "Dynamic Stall Control by Periodic Excitation, Part 1: NACA 0015 Parametric Study," *Journal of Aircraft*, Vol. 38, No. 3, May 2001, pp. 430–438.
doi:10.2514/2.2810

[10] Martin, P. B., Tung, C., Hassan, A. A., Cerchie, D., and Roth, J., "Active Flow Control Measurements and CFD on a Transport Helicopter Fuselage," *Proceedings of the American Helicopter Society 61st Annual National Forum*, Grapevine, TX, June 1–3 2005.

[11] Greenblatt, D., Darabi, A., Nishri, B., and Wygnanski, I., "Some Factors Affecting Stall Control with Particular Emphasis on Dynamic Stall," *Proceedings of 30th AIAA Fluid Dynamics Conference and Exhibit*, 99–3504, AIAA, Reston, VA, 1999.

[12] Rumsey, C. L., "Computation of a Synthetic Jet in a Turbulent Cross-Flow Boundary Layer," NASA Langley Research Center, Rept. 2004–213273, Hampton, Va, Oct. 2004.

[13] Di Cicca, G. M., and Iuso, G., "On Large-Scale Vortical Structures Produced by a Yawed Synthetic Jet: Turbulent Boundary Layer Interaction," *Proceedings of the 3rd AIAA Flow Control Conference*, 2006–2861, AIAA, Reston, VA, 2006.

[14] Milanovic, I. M., Zaman, K. B. M. Q., and Rumsey, C. L., "An Isolated Circular Synthetic Jet in Cross-Flow at Low Momentum-Flux Ratio," *Proceedings of the AIAA 43rd Aerospace Sciences Meeting & Exhibit*,

2005–1110, AIAA, Reston, VA, Jan. 10–13 2005.

[15] Schaeffler, N. W., "The Interaction of a Synthetic Jet and A Turbulent Boundary Layer," *Proceedings of the AIAA 41st Aerospace Sciences Meeting & Exhibit*, 2003-643, AIAA, Reston, VA, Jan. 6–9 2003.

[16] Smith, D. R., "Interaction of Synthetic Jet with a Crossflow Boundary Layer," *AIAA Journal*, Vol. 40, No. 11, Nov. 2002, pp. 2277–2288. doi:10.2514/2.1564

[17] Hassan, A. A., and Munts, E. A., "Traverse and Near-Tangent Synthetic Jets for Aerodynamic Flow Control," *Proceedings of the 18th AIAA Applied Aerodynamics Conference*, AIAA, Reston, VA, 2000, p. A00-39945.

[18] Milanovic, I. M., and Zaman, K. B. M. Q., "Highly Inclined Jets in Cross Flow," *Proceedings of the AIAA 41st Aerospace Sciences Meeting & Exhibit*, 2003–0183, AIAA, Reston, VA, 2003.

[19] Ekaterinaris, J. A., Chandrasekhara, M. S., and Platzer, M. F., "Recent Developments in Dynamic Stall Measurements, Computations and Control," *Proceedings of the AIAA 43rd Aerospace Sciences Meeting & Exhibit*, 2005–1296, AIAA Reston, VA, 2005.

[20] Ortmanns, J., and Kahler, C. J., "Investigation of Pulsed Actuator for Active Flow Control Using Phase Locked Stereoscopic Particle Image Velocimetry," *Proceedings of the 12th International Symposium Appl. Laser Tech. Fluid Mech*, Lisbon, Portugal, 2004.

[21] Chue, S. H., "Pressure Probes for Fluid Flow Measurements," *Progress in Aerospace Sciences*, Vol. 16, No. 2, 1975, pp. 147–223. doi:10.1016/0376-0421(75)90014-7

[22] Kreid, D. K., "Laser-Doppler Velocimeter Measurements in Nonuniform Flow Field: Error Estimates," *Applied Optics*, Vol. 13, No. 8, 1974, pp. 1872–1881. doi:10.1364/AO.13.001872

[23] Meunier, P., and Leweke, T., "Analysis and Treatment of Errors Due To High Velocity Gradients in Particle Image Velocimetry," *Experiments in Fluids*, Vol. 35, No. 5, 2003, pp. 408–421. doi:10.1007/s00348-003-0673-2

[24] Ramasamy, M., and Leishman, J. G., "Interdependence of Diffusion and Straining of Helicopter Blade Tip Vortices," *Journal of Aircraft*, Vol. 41, No. 5, Sept. 2004, pp. 1014–1024. doi:10.2514/1.3364

[25] Martin, P. B., Pugliese, G., and Leishman, J. G., "High Resolution Trailing Vortex Measurements in the Wake of a Hovering Rotor," *Proceedings of the American Helicopter Society 57th Annual National Forum*, Washington, D. C., May 9–11, 2001.

[26] Gilarranz, J. L., Yue, X., and Rediniotis, O. K., "PIV Measurements And Modeling of Synthetic Jet Actuator for Flow Control," *Proceedings of the 1998 ASME Fluids Engineering Division Summer Meeting*, Washington, D. C., 1998.

[27] Schaeffler, N. W., and Jenkins, L. N., "Isolated Synthetic Jet in Crossflow: Experimental Protocols for a Validation Dataset," *AIAA Journal*, Vol. 44, No. 12, Dec. 2006 pp. 2846–2856. doi:10.2514/1.13743

[28] Yao, C. S., Chen, F. J., and Neuhart, D., "Synthetic Jet Flow Field Database for Computational Fluid Dynamics Validation," *AIAA Journal*, Vol. 44, No. 12, Dec. 2006, pp. 3153–3157. doi:10.2514/1.13819

[29] Greenblatt, D., Paschal, K. B., Yao, C. S., and Harris, J., "A Separation Control CFD Validation Test Case Part 2: Zero Efflux Oscillatory Blowing," *Proceedings of 43rd AIAA Aerospace Sciences Meeting and Exhibit*, AIAA, Reston, VA, 2005.

[30] Klebanoff, P. S., "Characteristics of Turbulence in a Boundary Layer with Zero Pressure Gradient," NACA, Rept. NACA TN 1247, Washington, D.C., 1955.

[31] Ramasamy, M., and Leishman, J. G., "Benchmarking Particle Image Velocimetry with Laser Doppler Velocimetry for Rotor Wake Measurements," *AIAA Journal*, Vol. 45, No. 11, Nov. 2007, pp. 2622–2633. doi:10.2514/1.28130

[32] Scarano, F., and Riethmuller, M. L., "Iterative Multigrid Approach in PIV Image Processing with Discrete Window Offset," *Experiments in Fluids*, Vol. 26, No. 6, 1999, pp. 513–523. doi:10.1007/s003480050318

[33] Scarano, F., "Iterative Image Deformation Methods in PIV," *Measurement Science and Technology*, Vol. 13, No. 1, 2002, pp. R1–R19. doi:10.1088/0957-0233/13/1/201

[34] Hart, D. P., "Sparse Array Image Correlation," *8th International Symposium on Applications of Laser Techniques to Fluid Mechanics*, Lisbon, Portugal, July 8–11 1996.

[35] Theunissen, R., Scarano, F., and Riethmuller, M., "On Improvement of PIV Image Interrogation Near Stationary Interfaces," *Experiments in Fluids*, Vol. 45, No. 4, Oct. 2008, pp. 557–572. doi:10.1007/s00348-008-0481-9

[36] Honkanen, M., and Nobacj, H., "Background Extraction From Double-Frame PIV Images," *Experiments in Fluids*, Vol. 38, No. 3, March 2005, pp. 348–362. doi:10.1007/s00348-004-0916-x

[37] Martin, P. B., Pugliese, G., and Leishman, J. G., "Laser Doppler Velocimetry Uncertainty Analysis for Rotor Blade Tip Vortex Measurements," *38th AIAA Aerospace Sciences Meeting and Exhibit*, AIAA Paper CP 2000-0063, Reno, NV, Jan. 1997.

[38] Ligrani, P. M., Westphal, R. V., and Lemos, F. R., "Fabrication and Testing of Subminiature Multi-Sensor Hot- Wire Probes," *Journal of Physics E: Scientific Instruments*, Vol. 22, 1989, p. 262–268.

[39] DeGraaff, D. B., and Eaton, J. K., "Reynolds-Number Scaling of the Flat-Plate Turbulent Boundary Layer," *Journal of Fluid Mechanics*, Vol. 422, No. 1, 2000, pp. 319–346. doi:10.1017/S0022112000001713

[40] Sun, C., Cheung, Y., and Xia, K., "Experimental Studies of Viscous Boundary Layer Properties in Turbulent Rayleigh–Benard Convection," *Journal of Fluid Mechanics*, Vol. 605, No. 10, Oct. 2008, pp. 79–113.

[41] Blasius, H., "Laminare Stromung in Kanalen Wechselnder Breite," *Zeitschrift für Mathematik und Physik*, Vol. 110, 1910, pp. 58–90.

[42] Wu, J., "Near-Field Trajectory of Turbulent Jets Discharged at Various Inclinations into a Uniform Crossflow," *AIAA Journal*, Vol. 11, No. 11, 1973, pp. 1579–1581. doi:10.2514/3.50638